Nuclear Physics **A526** (1991) 1–35
North-Holland

NON-SPIN-FLIP (^{3}He, t) CHARGE-EXCHANGE AND ISOBARIC ANALOG STATES OF ACTINIDE NUCLEI STUDIED AT $\theta = 0°$, $E(^3\text{He}) = 76$ MeV AND 200 MeV

J. JÄNECKE[1], F.D. BECCHETTI[1], A.M. VAN DEN BERG[2], G.P.A. BERG[3], G. BROUWER[2], M.B. GREENFIELD[4], M.N. HARAKEH[5], M.A. HOFSTEE[2], A. NADASEN[6], D.A. ROBERTS[1], R. SAWAFTA[3], J.M. SCHIPPERS[2], E.J. STEPHENSON[3], D.P. STEWART[1] and S.Y. VAN DER WERF[2]

[1] *Department of Physics, University of Michigan, Ann Arbor, MI 48109, USA*
[2] *Kernfysisch Versneller Instituut, Zernikelaan 25, 9747 AA Groningen, The Netherlands*
[3] *Indiana University Cyclotron Facility, Bloomington, IN 47405, USA*
[4] *Department of Physics, Florida A&M University, Tallahassee, FL 32306, USA*
[5] *Faculteit Natuurkunde en Sterrenkunde, Vrije Universiteit, de Boelelaan 1081, 1081 HV Amsterdam, The Netherlands*
[6] *Department of Natural Sciences, University of Michigan, Dearborn, MI 48128, USA*

Received 4 October 1990

Abstract: The (^{3}He, t) charge-exchange reaction has been studied at $\theta = 0°$ and bombarding energies of $E(^3\text{He}) = 76.5$ MeV and 200 MeV. Spectra were measured using magnetic analysis for target nuclei of ^{12,13}C, ^{16}O, ^{19}F, ^{28,29,30}Si, ^{90}Zr, ^{117,120}Sn, ^{nat}Ta, ^{nat}W, ^{197}Au, ^{208}Pb, ^{230,232}Th, ^{234,236,238}U and ^{244}Pu. The measurements at 76.5 MeV concentrated on the isobaric analog states of several actinide nuclei, particularly on their widths and the branching ratios for proton decay. Cross sections, Q-values and total widths were determined for the transitions to the isobaric analog states. Coulomb displacement energies derived from the measured Q-values display the influence of deformed nuclear shapes. Escape widths $\Gamma^{\uparrow}$ and spreading widths $\Gamma^{\downarrow}$ of the isobaric analog states in five actinide nuclei were deduced from the measured proton-decay branching ratios. They were found to be in agreement with predictions which postulate isospin mixing via the Coulomb force with the $(T_0 - 1)$-component of the isovector giant monopole resonance. The measurements at 200 MeV were concerned with transitions to isobaric analog states in both light and heavy nuclei, including several actinide nuclei, but Gamow-Teller resonances and transitions to numerous other states were also observed. The measured cross sections for several transitions to isobaric analog states from ^{30}Si to ^{208}Pb were used to extract the effective interaction V_τ for non-spin-flip (^{3}He, t) charge exchange at $E(^3\text{He}) \approx 200$ MeV. The interaction strength V_τ decreases by a factor 0.6 when compared to previously measured values for the energy range $E(^3\text{He}) = 65$ to 90 MeV. An angular distribution from $\theta_t = 0°$ to 16° for the transition to the isobaric analog state in ^{120}Sb measured at $E(^3\text{He}) = 200$ MeV was found to be in very good agreement with microscopic calculations.

E

NUCLEAR REACTIONS ^{12}C, ^{16}O, ^{27}Al, ^{28}Si, Ta, ^{230}Th, ^{232}Th, ^{234}U, ^{236}U, ^{238}U (^{3}He, t), $E = 76.5$ MeV ^{12}C, ^{13}C, ^{16}O, ^{19}F, ^{28}Si, ^{29}Si, ^{90}Zr, ^{117}Sn, ^{120}Sn, Ta, W, ^{197}Au, ^{208}Pb, ^{230}Th, ^{232}Th, ^{234}U, ^{238}U, ^{244}Pu (^{3}He, t), $E = 200$ MeV; measured σ (E_t) $\theta_t = 0°$; ^{120}Sn (^{3}He, t), $E = 200$ MeV; measured $\sigma(\theta_t)$ for isobaric analog state (IAS), $\theta_t = 0°$ to 16°; ^{230}Th, ^{232}Th, ^{234}U, ^{236}U, ^{238}U (^{3}He, tp), $E = 76.5$ MeV; measured proton decay from IAS, $\sigma(E_t, E_p, \theta_t, \theta_p)$ for $\theta_t = 0°$, $\theta_p = +120°$, +150°, −150°; deduced Q-values for transitions to IAS, ^{90}Nb, ^{117}Sb, ^{120}Sn, ^{181}W, ^{184}Re, ^{197}Hg, ^{208}Pb, ^{230}Pa, ^{232}Pa, ^{234}Np, ^{236}Np, ^{238}Np, ^{244}Am, Coulomb displacement energies, total widths Γ, escape widths $\Gamma^{\uparrow}$, spreading widths $\Gamma^{\downarrow}$ of IAS, ^{208}Pb, ^{230}Pa, ^{232}Pa, ^{234}Np, ^{236}Np, ^{238}Np, ^{244}Am. Effective interaction V_τ for non-spin-flip charge exchange transitions to IAS, ^{30}P, ^{90}Nb, ^{120}Sn, ^{208}Pb. Enriched and long-lived radioactive targets; magnetic spectrometers.

1. Introduction

The (^{3}He, t) reaction, similar to the (p, n) reaction [1,2]), is a very powerful tool to study both non-spin-flip and spin-flip charge-exchange leading to isobaric analog states (IAS), to other sharp states, and to Gamow-Teller and other resonances possibly including the isovector giant monopole resonance (IVGMR). Emphasis on the observation of $L = 0$ transitions requires measurements at $\theta_t = 0°$. A special setup is needed for the (p, n) reaction where the neutron detectors are located at or near 0°. After interacting with the target the proton beam must be deflected away from 0° and stopped in a well-shielded beam dump. In contrast, the use of a magnetic spectrograph is essential for measuring at 0° in the (^{3}He, t) reaction. Here, the techniques for obtaining background-free spectra when the beam of projectiles enters the magnetic spectrometer at 0° are critical and have to be perfected. This is particularly important for measurements at $E(^3\text{He}) \approx 200$ MeV. Investigations at lower bombarding energies and $\theta_t = 0°$ using (^{3}He, t) to study isobaric analog and other states have been performed for many years [3-11]) including coincidence measurements with decay protons [7-10]) and fission products [4]).

Non-spin-flip transitions dominate at low bombarding energies, and the discovery of IAS was in fact made [12]) in low-energy (p, n) charge exchange. The usefulness of the (p, n) and (^{3}He, t) reactions for studying either non-spin-flip or spin-flip phenomena requires an understanding of the dependence on bombarding energy of the various contributions to the charge-exchange reaction mechanism. This is quite well understood for the (p, n) reaction [e.g. ref. [13])], but less well for (^{3}He, t) [e.g. refs. [11,14-17])] with little information available in the range $E(^3\text{He}) = 100$ to 600 MeV.

The primary objective of the present work was to observe and study IAS from several long-lived radioactive actinide targets. Only very limited data exist for IAS of targets with masses greater than ^{208}Pb. The measurement of precise Q-values leads to Coulomb displacement energies ΔE_{Coul} for comparison with predictions based on shell-model and other equations [18,19]). Deformed nuclear shapes including quadrupole and hexadecapole deformation, β_2 and β_4, are expected to lead to a reduction in ΔE_{Coul} of the order of 150 keV.

The various decay modes of IAS (proton decay, neutron decay, also fission decay in the actinide nuclei) are responsible for a finite IAS line width Γ with lorentzian line shape. Measuring the branching ratios for proton decay and/or the other IAS decay modes makes it possible to determine the two components of Γ, the spreading width $\Gamma^{\downarrow}$ and the escape with $\Gamma^{\uparrow}$, for comparison with predictions [20,21]). These widths are of particular interest for the actinide nuclei where only very limited data including decay data exist. A good understanding of the global behavior of the spreading width $\Gamma^{\downarrow}$ for medium-heavy and heavy nuclei in terms of isospin mixing of the IAS with the $T_<$-component of the isovector giant monopole resonance (IVGMR) has recently been achieved [20]). A splitting of this resonance in deformed

nuclei due to mixing with the beta-vibration component of the isovector giant quadrupole resonance (IVGQR) has been postulated, and data for the actinide nuclei provide a test of the predictive power of these calculations. Independently, a phenomenological expression [22]) has also been used to describe the observed increase of $\Gamma^{\downarrow}$ with neutron excess. A new expression for the escape widths $\Gamma^{\uparrow}$ has been derived recently [21]), and a quantatitive comparison between experimental and calculated values has become possible.

The following sects. 2 and 3 describe the experimental procedures and aspects of the data reduction and energy calibration. The experimental results obtained at the two bombarding energies are presented in sect. 4. These include the zero-degree spectra for light and heavy target nuclei, the proton decay coincidence data (^{3}He, t$\bar{p}$) obtained at $E(^3\text{He}) = 76.5$ MeV for the actinide targets, and the angular distribution measured for ^{120}Sn (^{3}He, t) ^{120}Sb (IAS) at $E(^3\text{He}) \approx 200$ MeV. The discussion in sect. 5 includes a comparison of the measured Coulomb displacement energies and the total, escape, and spreading widths of IAS in actinide nuclei with predictions, and a determination of the effective (^{3}He, t) charge-exchange interaction V_τ from measured IAS cross sections at $E(^3\text{He}) = 200$ MeV. This includes a microscopic DWBA analysis of the angular distribution for the transition to the IAS in ^{120}Sb. A short summary follows in sect. 6.

2. Experimental procedures

2.1. 200 MeV EXPERIMENT

The experiment utilized a beam of 200 MeV $^3\text{He}^{++}$ particles from the Indiana University Cyclotron Facility (IUCF). The measurements were carried out with a high-resolution magnetic spectrometer. Fig. 1 shows a schematic diagram of the spectrometer with the target in the scattering chamber, the focal-plane detector system, the internal $^3\text{He}^{++}$ beam stop and the trajectories for incoming and outgoing particles. Upon entering the magnetic spectrograph at $\theta = 0°$, the beam was bent inward where it hit an electrically insulated graphite beam stop inside the first dipole magnet. The beam current ranged from 20 to 80 nA (electrical). The current reading from the beam stop was tested against an external Faraday cup.

Tritons from the (^{3}He, t) reaction on various targets were detected in the focal plane of the IUCF K600 magnetic spectrograph [23]). The focal-plane detection system [24]) consisted of two multi-wire drift chambers backed by two scintillation detectors of thicknesses 6 mm and 12 mm for particle identification and drift-time measurements.

Background from reaction products in the beam stop inside the first dipole magnet could be suppressed by optimizing the position of the appropriately designed beam stop. Software gating on signals supplied by the two-dimensional position sensitive detector in the focal plane such as energy loss in the scintillators, and angle of

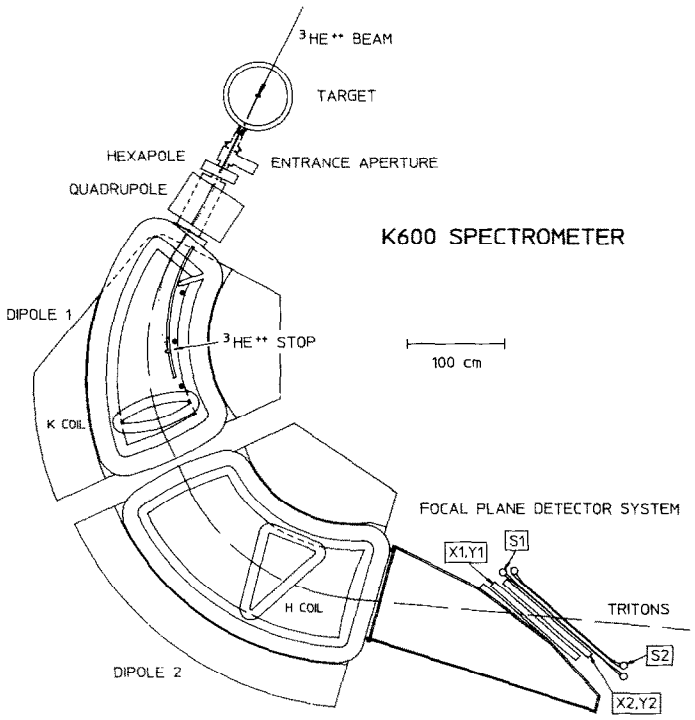

Fig. 1. Schematic diagram of the IUCF K600 spectrograph used for zero-degree measurements at $E(^3\mathrm{He}) = 200$ MeV.

incidence was also employed. Background from reactions in the target frame induced by low-momentum beam halo which occurs on one side of the beam was greatly reduced by using non-symmetric U-shaped target frames.

Beams with reduced beam halo had to be used for the thin actinide targets which were mounted on frames with circular openings of only 12 or 9 mm diameter. The effective length of the focal-plane detector was 80 cm covering an energy range of $\Delta E/E \approx 16\%$ ($\Delta E > 30$ MeV). The magnetic field was kept constant for all measurements. Most measurements were made with a circular aperture with a solid angle of $\Delta\Omega \approx 4$ msr. A rectangular aperture centered at 1° was used in a few instances to allow the independent measurement of 0° and 2° spectra and cross sections. A smaller aperture with a solid angle of $\Delta\Omega \approx 1.0$ msr was used at $\theta_t > 5°$ to measure an angular distribution.

2.2. 76 MeV EXPERIMENT

A beam of 76.5 MeV $^3\mathrm{He}^{++}$ particles from the KVI cyclotron was used for the (^{3}He, t$\bar{\mathrm{p}}$) coincidence measurements on the actinide targets. The experimental setup was similar to the one used previously for the measurements of other IAS and their

decays [e.g. ref. [9])] except for the use of an improved focal-plane detection system [25]). The beam entered the magnetic spectrograph at $\theta = 0°$ and was stopped in a graphite block which served as a Faraday cup. It was mounted at the end of an aluminum rod on the inside of the first dipole magnet. The beam current was typically 20 nA. Tritons from the (^{3}He, t) reaction on various targets have higher magnetic rigidity than the incoming $^3He^{++}$ beam. They were detected in the focal-plane of the QMG/2 magnetic spectrograph [26]) with a solid angle of $\Delta\Omega = 6$ msr and a focal plane detection system [25]) consisting of a multi-wire drift chamber backed by a sintillation detector of thickness 3 mm for particle identification. The effective length of 90 cm of the detector covered a useful energy range of $\Delta E/E \approx 12\%$ ($\Delta E \approx 9$ MeV). The magnetic field was kept constant for all measurements.

The proton-decay data were obtained by measuring tritons reaching the focal-plane detector in coincidence with protons detected in any of three 5 mm thick Li-drifted Si detectors of effective area 250 mm^2 each. These detectors were mounted at angles of +120°, +150° and −150° with respect to the beam direction. The combined solid angle was $\Delta\Omega = 220$ msr. The detectors were cooled with an alcohol refrigerating unit. They were covered with Ni foils of thicknes 0.3 mg/cm^2 to prevent condensation of oil and other vapors on their surfaces and to stop shake-off electrons from the target. The time difference between the arrival of protons in the Si detectors and tritons in the focal-plane detector made it possible to distinguish between prompt and random coincidences.

TABLE 1

Targets (200 MeV)	$\rho\Delta x$ (mg/cm^2)	Targets (76.5 MeV)	$\rho\Delta x$ (mg/cm^2)
^{nat}C	0.384	^{nat}C	0.174
$^{nat}WO_3$	0.237 on 0.205 Au	$^{nat}Ta_2O_3$	0.50
^{nat}Si	0.225	^{nat}Si	0.20
^{90}Zr	1.04	$^{230}ThO_2$ [c]) (99.86%)	0.424 on 0.205 Al
^{120}Sn	2.17	^{nat}Th [c])	0.680
^{nat}Ta	0.60	^{234}U acetate [c]) (99.077%)	0.514 on 0.205 Al
^{208}Pb	0.65	^{236}U acetate [c,d]) (99.63%)	0.752 on 0.205 Al
$^{230}ThO_2$ [a])	~0.05 on 0.05 C	$^{nat}UF_4$ [c])	0.545 on 0.205 Al
^{nat}Th	1.90		
$^{nat}ThF_4$ [b])	0.35 on 0.05 C		
$^{234}UO_2$ [a])	~0.05 on 0.05 C		
$^{236}UO_2$ [a])	~0.05 on 0.05 C		
$^{nat}UF_4$ [b])	0.33 on 0.05 C		
$^{244}PuO_2$ [a])	~0.05 on 0.05 C		

[a]) Targets obtained from Physics Division, Argonne National Laboratory.
[b]) Targets obtained from Micromatter Co., Deer Harbor, WA 98243.
[c]) Targets obtained from Euratom Research Center, Geel, Belgium.
[d]) Target broken and repaired.

2.3. TARGETS

The targets used in the two experiments are listed in table 1. The self-supporting ^{208}Pb target and the natural thorium foil used in the 200 MeV experiment were stored under vacuum and contained traces of oxygen contaminants. Targets of natural thorium and uranium fluoride were deposited on carbon backings. The other actinide targets used at IUCF were rather thin, backed by carbon and mounted on relatively small frames. The actinide targets used at the KVI were typically 0.5 mg/cm^2 thick. They were obtained as oxide, fluoride, or by spraying acetate soution on a thin backing of aluminum. The acetate decomposed under bombardment but converted to the oxide and remained a useful target. All radioactive actinide targets used for the coincidence measurements had isotopic abundances greater than 99%. The uncertainties in target thicknesses for the thin actinide targets used at IUCF are estimated at ±50% but at less than ±10% for all other targets.

3. Data reduction and energy calibration

3.1. DATA REDUCTION

Position signals from the IUCF focal-plane detector were obtained by measuring the drift times from neighboring wires and then calculating the position. The triton particle identification for this detector was provided by the two scintillators mounted behind the wire chambers. This gave clean particle identification signals, particularly due to the fact that the high magnetic field setting of the spectrograph prevented protons, deuterons, and ^{3,4}He^{++} particles produced in the target from reaching the detector. A second gate was set on the angles of incidence of the particles relative to the focal plane. Projected triton spectra using these gates are presented in sect. 4.

The position information for the KVI focal plane detector was obtained similarly by determining the drift times for neighboring wires. The triton particle-identification signal for the KVI focal plane detector was obtained from one scintillator in combination with timing information for the arrival of the tritons in the focal plane relative to the RF. The energy loss signal from the scintillator and the time-of-flight of the particles through the spectrometer differ with particle type and can therefore be used for particle identification. Another gate was set on the angles of incidence on the focal-plane detector. Projected triton spectra are presented in sect. 4.

Spectra obtained for ^{12}C, ^{16}O and ^{28}Si served primarily for energy calibration (see below). Furthermore, lines from ^{12}C backings and from ^{16}O contaminants in the targets were present in some of the spectra for the heavier targets. Spectra corrected for contaminants were obtained for some of these cases by subtracting properly normalized spectra from the carbon and oxygen targets.

The transitions to the analog states in ^{29}P ($\frac{1}{2}^+$, g.s.) and ^{30}P (0^+, 677 keV) are nearly degenerate in energy. Unfolding of the observed, slightly broadened line became possible by fitting it with two gaussian distributions with fixed centroid energies.

The latter were obtained from a careful energy calibration. The cross sections so obtained were subsequently used to extract an effective interaction V_τ (see sub-sect. 5.3).

Several of the zero-degree spectra obtained at 200 MeV were measured with rectangular apertures centered at 1°. Ray tracing was then used to extract two separate spectra centered at angles $\theta_t \approx 0°$ and 2°. This procedure was employed in obtaining two forward-angle data points for the angular distribution from the ^{120}Sn target.

The data for the actinide targets obtained at $E(^3\text{He}) = 76.5$ MeV in coincidence with decay protons were given special attention. Fig. 2 displays the spectrum for the time difference between the arrival of protons in one of the Si detectors and tritons in the focal-plane detector. The spectrum displays the presence of random coincidences with every beam burst separated by ~100 ns, and the presence of a single much more intense (factor ×8) prompt peak. The true coincidence events are represented by the difference of prompt minus random events. Fig. 3 shows as example a two-dimensional display of prompt events for ^{234}U(^{3}He, tp̄)^{233}U representing proton energy versus triton energy. Very clean projected triton spectra for the transition to the final heavy nucleus can be extracted from this information (see below). These spectra serve as a basis for the determination of total widths Γ from the lorentzian line shape and for the determination of branching ratios for proton decay from the relative yield.

3.2. ENERGY CALIBRATION

The reactions ^{12}C(^{3}He, t)^{12}N, ^{16}O(^{3}He, t)^{16}F and ^{28}Si(^{3}He, t)^{28}P were measured several times during the running period to provide energy calibrations for the 200 MeV and 76.5 MeV experiments (see figs. 4-6). The respective Q-values and

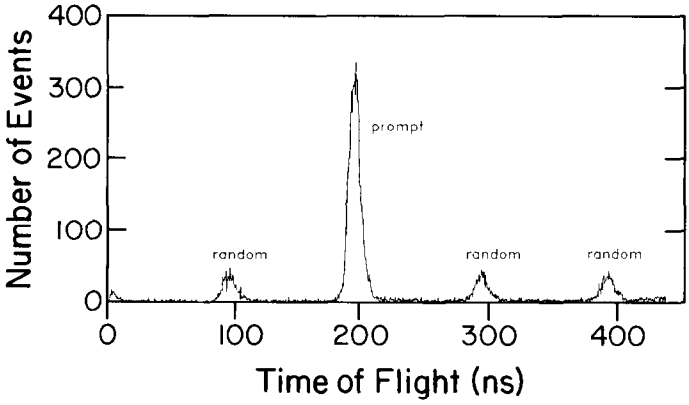

Fig. 2. Time-of-flight for the arrival of protons from the reaction ^{234}U(^{3}He, tp̄)^{233}U in the Si detector relative to the arrival of tritons in the focal plane. Beam bursts are separated by ~100 ns.

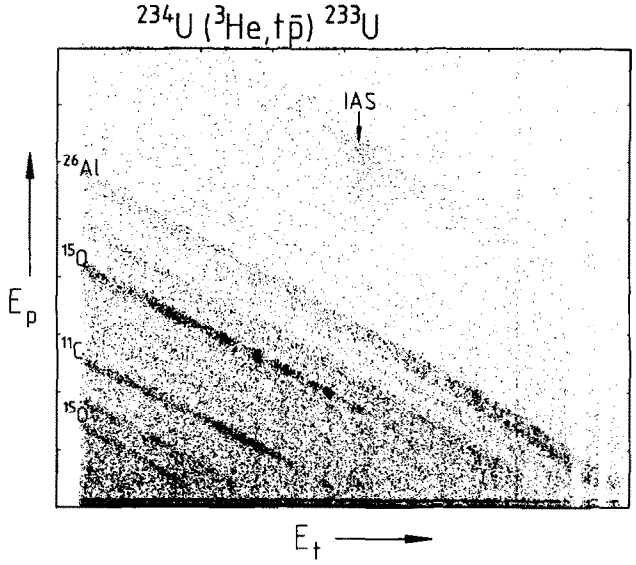

Fig. 3. Two-dimensional scatter plot of proton energy E_p versus triton energy E_t of prompt coincidence events for the reaction ^{234}U(^{3}He, tp̄) ^{233}U. The energy ranges are about 0 to 15 MeV for E_p and 52 to 61 MeV for E_t.

excitation energies with uncertainties were taken from refs. [27-30]). Selected strong lines from backing materials and from contaminants also provided convenient calibration points which made it possible to estimate stability and drift during the running period.

A systematic apparent energy drift of about 150 keV was observed during the 200 MeV experiment probably due to a drift in the K600 magnetic field. However, the presence of ^{12}C and ^{16}O contaminants in most targets made it possible to follow this drift very closely, and the energy calibration is reproducible to within ±12 keV. No such drift was observed for the 76.5 MeV experiment except for one discrete change of about 50 keV before the last run with the ^{236}U target. Here again, the presence of lines from ^{16}O provided a reliable calibration. The energy calibration for the 76.5 MeV data is believed to be reproducible to within ±8 keV due to the uncertainties of the Q-values and excitation energies of the calibration lines.

4. Experimental results

4.1. SPECTRA

Figs. 5-9 display selected spectra obtained for the various targets at $\theta_t = 0°$ for $E(^3\text{He}) = 200$ MeV. The fixed spectrograph setting allowed the observation of tritons

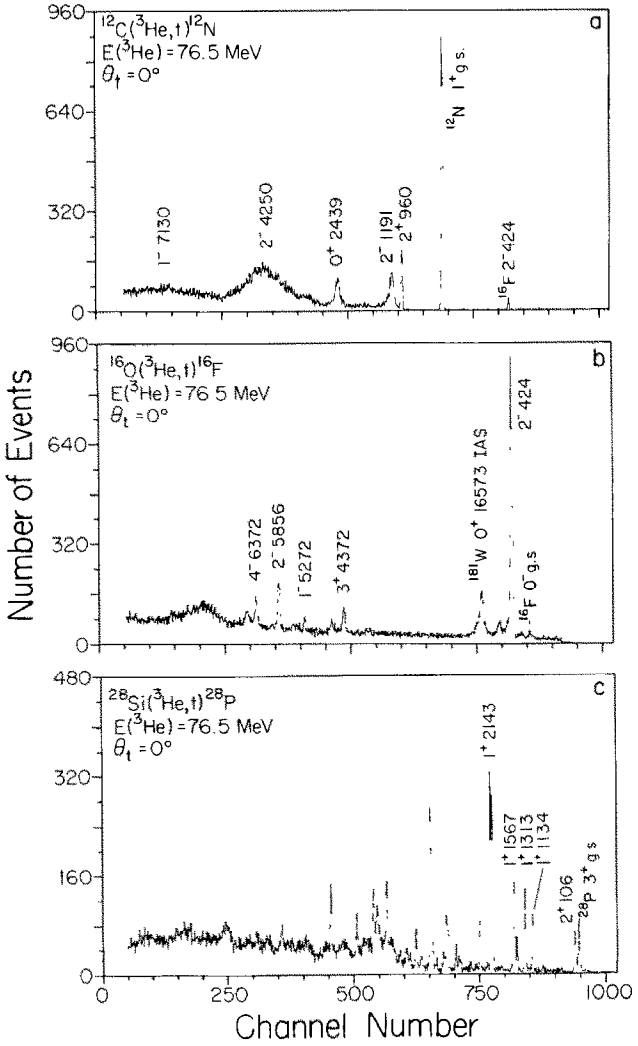

Fig. 4. Triton energy spectra from the (^{3}He, t) reaction obtained with the QMG/2 magnetic spectrograph (KVI) at $E(^3\text{He}) = 76.5$ MeV and $\theta_t = 0°$ and identical magnetic field settings for targets of (a) ^{nat}C, (b) Ta_2O_3, (c) ^{nat}Si. Excitation energies are given in keV.

ranging from 169 MeV to 202 MeV as shown in figs. 5, 7 and 8. Depending on the Q-value for the ground-state transition, excitation energies for the residual nuclei ranging from a few MeV to 25 MeV could be studied. Figs. 6 and 9 display expanded regions for selected spectra. Corrected spectra for IAS in actinide nuclei are shown in fig. 10 with lorentzian line-shape fitting. The energy resolution in the focal plane was about 50 keV FWHM due to the finite spectrograph and detector resolution

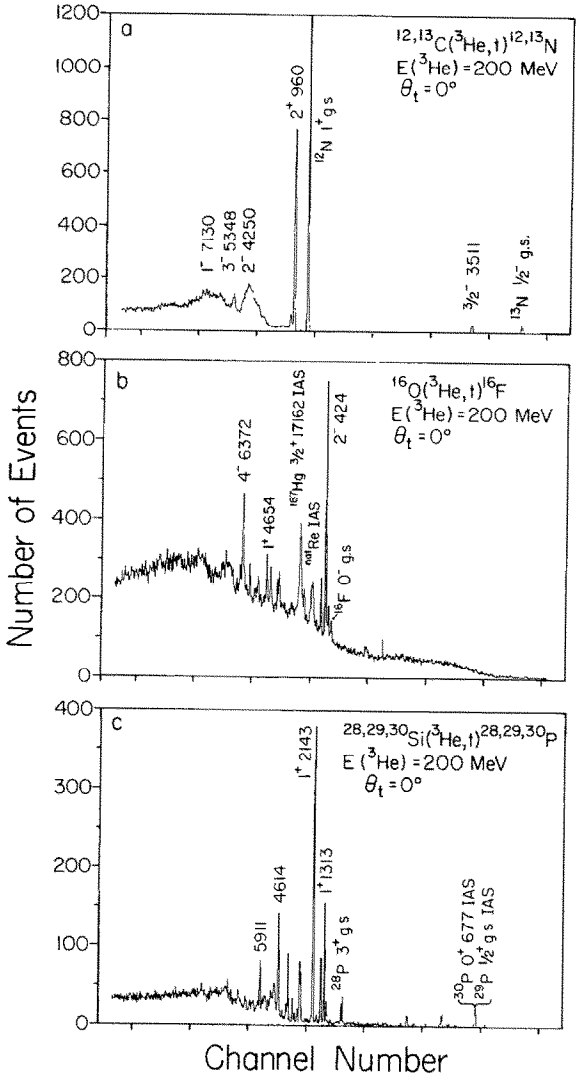

Fig. 5 Triton energy spectra from the (^{3}He, t) reaction obtained with the K600 magnetic spectrograph (IUCF) at $E(^3\text{He}) = 200$ MeV and $\theta_t = 0°$ and identical magnetic field settings for targets of (a) ^{nat}C, (b) WO_3 on Au, (c) ^{nat}Si. Excitation energies are given in keV.

and the energy loss in the targets with thicknesses of tyically 0.5 mg/cm^2 (see subsect. 2.3). Cross sections, Q-values and excitation energies for IAS and other states derived from these data are included in tables 2 and 3. The light nuclei were chosen for energy calibration. They also permit a subtraction procedure to correct for contributions in other targets from the backing or from contaminants (carbon and

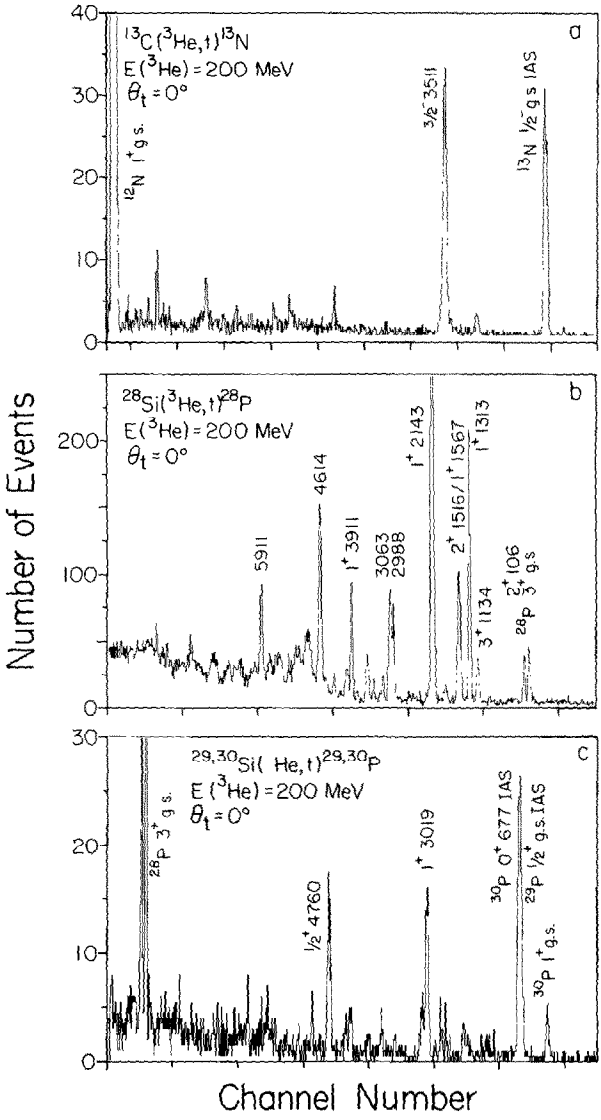

Fig. 6. Triton enegy spectra (expanded scales) for the (^{3}He, t) reaction at $E(^3\text{He}) = 200$ MeV and $\theta_t = 0°$ for targets of (a) ^{nat}C/^{13}C, (b) ^{nat}Si/^{28}Si, (c) ^{nat}Si/^{29,30}Si. Excitation energies are given in keV.

oxygen). The angular distribution obtained for the transition to the IAS in ^{120}Sn (fig. 7b) is described in subsect. 4.2. below.

Fig. 7a displays a triton energy spectrum for the ^{90}Zr target at $E(^3\text{He}) = 200$ MeV. It also shows a line which is due to singly-ionized $^3\text{He}^+$ particles reaching the focal plane directly from the target. They are the result of atomic charge exchange of the

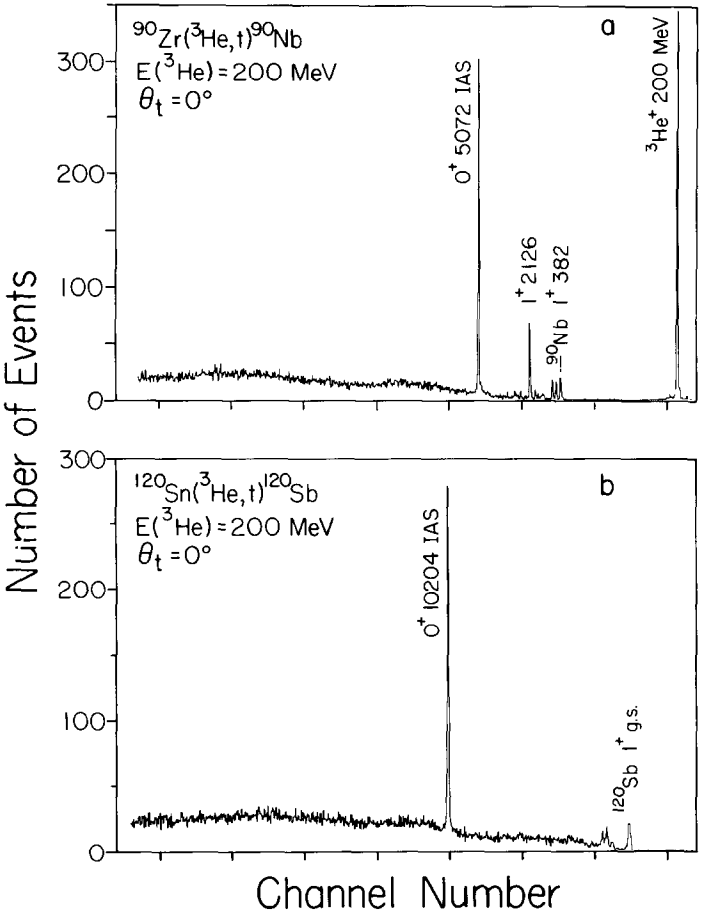

Fig. 7. Triton energy spectra from the (^{3}He, t) reaction of $E(^3\text{He}) = 200$ MeV and $\theta_t = 0°$ for targets of (a) ^{90}Zr, (b) ^{120}Sn. Excitation energies are given in keV.

incident $^3He^{++}$ beam in the target material. Although the ratio of $^3He^+/^3He^{++}$ is exceedingly small, and furthermore only a small fraction of these events are recorded within the triton identification gates, they still produce a dominant peak in the spectrum of fig. 7a because of the large number of incident particles.

The total number of $^3He^+$ particles is only about 4×10^{-9} of the incident $^3He^{++}$ beam. Nevertheless, these events increased the count rate in the focal plane detector by typically 50%. A moveable absorber mounted in the focal plane was therefore used for most other runs to block out the $^3He^+$ particles.

The spectra obtained at $\theta_t = 0°$ for $E(^3\text{He}) = 76.5$ MeV are displayed in figs. 4 and 11. A more limited range of excitation energies of about 9 MeV near the IAS was measured for the actinide targets with triton energies ranging from about 52 to 61 MeV. The energy resolution was about 60 keV due mostly to target thickness.

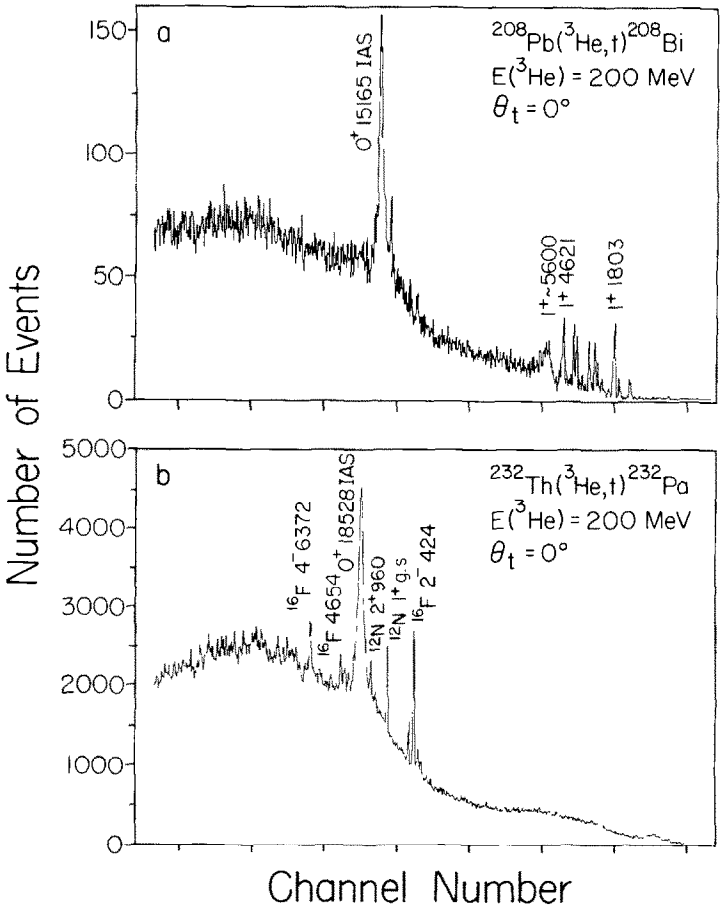

Fig. 8. Triton energy spectra from the (^{3}He, t) reaction at $E(^3\text{He}) = 200$ MeV and $\theta_t = 0°$ for targets of (a) ^{208}Pb, (b) ^{nat}Th. Excitation energies are given in keV.

The spectra for the light target nuclei were again obtained for energy calibration and to allow an estimate of the contributions from backings and contaminants to the spectra of the other targets. The subtraction method was successfully employed. The measured cross sections, Q-values and excitation energies for the IAS and a few other states are listed in tables 2 and 3. The spectra and data obtained for the actinide targets in coincidence with decay protons are described in subsect. 4.3. below.

4.1.1. $^{12}C(^3He, t)^{12}N$. The spectra obtained at $E(^3\text{He}) = 76.5$ MeV and 200 MeV are shown in figs. 4a and 5a, (see also fig. 9b). They are both dominated by the strong transition to the 1^+ ground state in ^{12}N. The 2^+ state at 0.960 MeV is also strong at both energies. The weakness of the 0^+ state at 2.439 MeV for $E(^3\text{He}) =$ 200 MeV is surprising considering its $L = 0$ character.

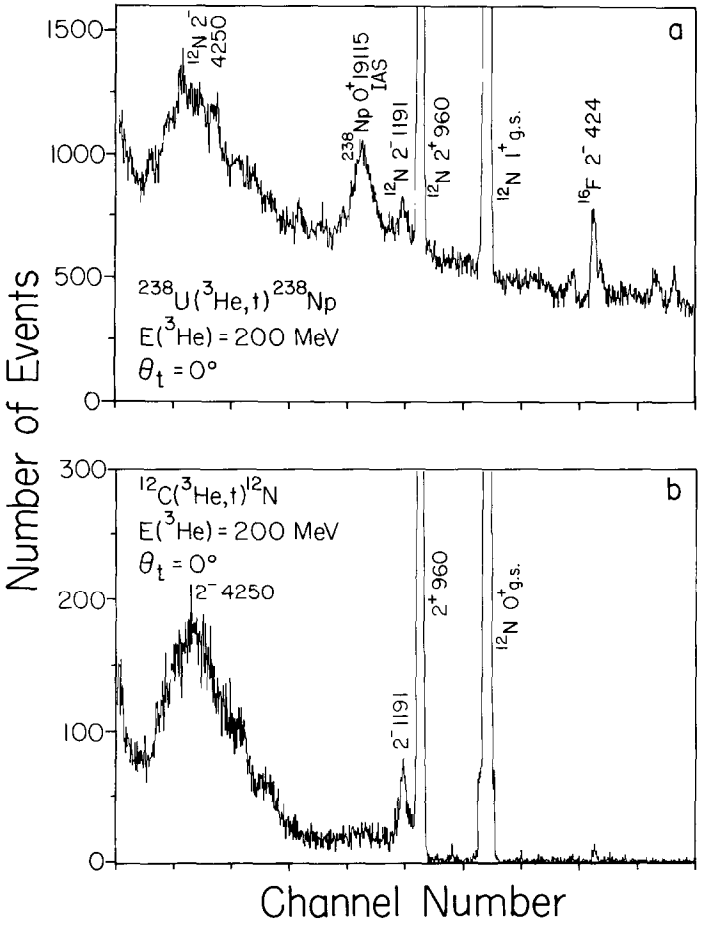

Fig. 9. Triton energy spectra (expanded scales) from the (^{3}He, t) reaction at $E(^3\text{He}) = 200$ MeV and $\theta_t = 0°$ for targets of (a) $^{nat}UF_4$, (b) $^{nat}C/^{12}C$. Excitation energies are given in keV.

4.1.2. $^{13}C(^3He, t)^{13}N$. The isotopic abundance of 1.1% of ^{13}C in natural carbon and the much more positive Q-value are responsible for the two weak lines seen in fig. 5a at higher triton energy. An expanded spectrum is shown in fig. 6a. The mirror transition to the $\frac{1}{2}^-$ ground state of ^{13}N, an IAS, and the Gamow-Teller transition to the $\frac{3}{2}^-$ state at $E_x = 3.511$ MeV are approximately equal in strength.

4.1.3. $^{16}O(^3He, t)^{16}F$. The spectra shown in figs. 4b and 5b were obtained at $E(^3\text{He}) = 76.5$ MeV and 200 MeV and with targets of Ta_2O_3 and WO_3 on Au backing, respectively. Several ^{16}F states are clearly recognizable, in particular the 0^-, 1^-, 2^-, 3^- ground-state multiplet with the 2^- state by far the strongest, as well as the 4^- state at 6.372 MeV. They provide convenient energy calibration lines. An essentially continuous background from Ta, W and Au in the target is also seen, as are the IAS of Ta, Au and W. The latter is broadened because of the number of stable W isotopes.

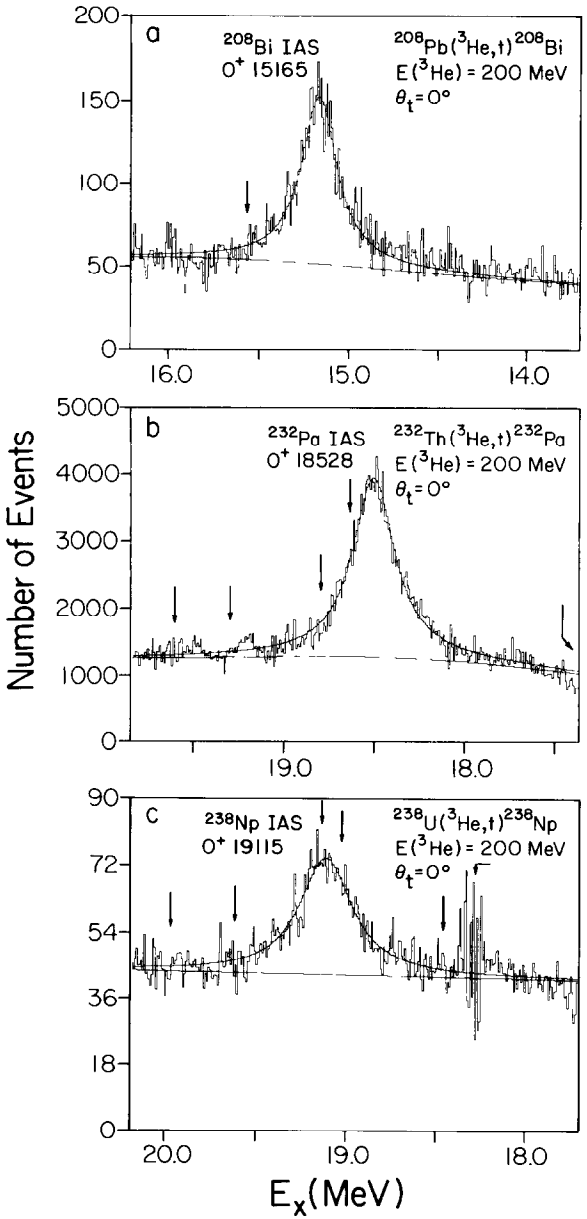

Fig. 10. Triton energy spectra (expanded scales) corrected for background obtained for the IAS in (a) ^{208}Bi, (b) ^{232}Pa and (c) ^{238}Np at $E(^3\text{He}) = 200$ MeV, $\theta_t = 0°$ with lorentzian line shape fitting. Irregular patterns appear where contributions from ^{12}C and ^{16}O contaminants are subtracted. The locations are marked by arrows.

TABLE 2a

Zero-degree cross section $d\sigma/d\Omega$ for (^{3}He, t) transitions to isobaric analog and other states in light nuclei

Target nucleus	Final nucleus	E_x [a] (keV)	J^π	$d\sigma/d\Omega$ (0°; 200 MeV) [c] (mb/sr)
^{12}C	^{12}N	0	1^+	3.77 ± 0.03
		960	2^+	1.11 ± 0.02
		1191	2^-	0.142 ± 0.005
		2439	0^+	0.011 ± 0.004
^{13}C	^{13}N	0	$\frac{1}{2}^-$ (IAS)	7.80 ± 0.34
		3511	$\frac{3}{2}^-$	9.32 ± 0.38
^{16}O	^{16}F	0	0^-	0.031 ± 0.003
		192	1^-	0.052 ± 0.004
		424	2^-	0.325 ± 0.006
		721	3^-	0.077 ± 0.004
		3758	1^+	0.056 ± 0.005
		3870	2^+	0.070 ± 0.005
		4372	3^+	0.048 ± 0.004
		4658	1^+	0.075 ± 0.005
		5272	(1^-)	0.100 ± 0.006
		5856	2^-	0.049 ± 0.005
		6372	4^-	0.217 ± 0.008
^{19}F	^{19}Ne	0	$\frac{1}{2}^+$ (IAS)	3.68 ± 0.02
		275	$\frac{1}{2}^-$	0.302 ± 0.004
^{28}Si	^{28}P	0	3^+	0.047 ± 0.003
		106	2^+	0.039 ± 0.003
		1134	3^+	0.042 ± 0.003
		1313	1^+	0.209 ± 0.006
		1516	2^+	
		1567	1^+	0.167 ± 0.006
		2143	1^+	0.688 ± 0.012
		2988 ± 25 [b]		0.088 ± 0.004
		3063 ± 25 [b]		0.140 ± 0.006
		3911	1^+	0.102 ± 0.005
		4614 ± 25 [b]		0.232 ± 0.016
		5911 ± 25 [b]		0.113 ± 0.006
^{29}Si	^{29}P	0	$\frac{1}{2}^+$ (IAS)	0.383 ± 0.064
		1384	$\frac{3}{2}^+$	0.110 ± 0.022
		2423	$\frac{3}{2}^+$	0.152 ± 0.026
		3448	$\frac{7}{2}^-$	0.114 ± 0.022
		4760	$\frac{1}{2}^+$	0.643 ± 0.053
^{30}Si	^{30}P	0	1^+	0.268 ± 0.042
		677	0^+ (IAS)	1.49 ± 0.13
		3019	1^+	0.91 ± 0.08
		4945	1^+	0.273 ± 0.048

[a]) Excitation energies from the literature unless noted otherwise. [$A = 12, 13, 16, 19$; ref. [27])], [$A = 28, 29, 30$; ref. [28])], [$A = 28$; ref. [29])].

[b]) Present work.

[c]) Cross section measured with a circular aperture centered at 0° with $\Delta\Omega = 3.43$ msr. The average angle is $\theta \approx 1.4°$ assuming a flat angular distribution.

TABLE 2b

Zero-degree cross section $d\sigma/d\Omega$ for (^{3}He, t) transitions to isobaric analog and other states in medium-heavy and heavy nuclei

Target nucleus	Final nucleus	E_x [a] (keV)	J^π	$d\sigma/d\Omega$ (0°; 76.5 MeV) (mb/sr)	$d\sigma/d\Omega$ (0°; 200 MeV) [c] (mb/sr)
^{90}Zr	^{90}Nb	382	1^+		0.314 ± 0.023
		651	3^+		0.258 ± 0.021
		854	(2^+)		0.234 ± 0.020
		2126	1^+		1.05 ± 0.04
		5072 ± 25 [b]	0^+ (IAS)		3.91 ± 0.08
^{117}Sn	^{117}Sb	11 271 [f]	$\frac{1}{2}^+$ (IAS)		4.37 ± 0.08 [d]
^{120}Sn	^{120}Sb	0	1^+		0.639 ± 0.033 [d]
		10 204	0^+ (IAS)		4.92 ± 0.08 [d]
^{181}Ta	^{181}W	16 573 [e]	$\frac{7}{2}^+$ (IAS)		
^{197}Au	^{197}Hg	17 162 ± 15 [b]	$\frac{3}{2}^+$ (IAS)		1.21 ± 0.03
^{208}Pb	^{208}Bi	1803 ± 25 [b]	1^+		0.302 ± 0.015 [d]
		3174 ± 25 [b]	1^+		0.204 ± 0.014 [d]
		3863 ± 25 [b]	1^+		0.194 ± 0.013 [d]
		4043 ± 25 [b]	1^+		0.173 ± 0.013 [d]
		4621 ± 25 [b]	1^+		0.350 ± 0.018 [d]
		~5600 [b]	1^+ (broad)		
		15 165 [f]	0^+ (IAS)		2.43 ± 0.07 [d]
^{230}Th	^{230}Pa	17 763 ± 18 [b]	0^+ (IAS)	10.8 ± 0.8	~3.0
^{232}Th	^{232}Pa	18 528 ± 11 [b]	0^+ (IAS)	15.7 ± 1.0	3.73 ± 0.04
^{234}U	^{234}Np	17 608 ± 12 [b]	0^+ (IAS)	7.2 ± 0.8	
^{236}U	^{236}Np	18 433 ± 57 [b]	0^+ (IAS)	9.3 ± 1.3	
^{238}U	^{238}Np	19 115 ± 8 [b]	0^+ (IAS)	9.1 ± 0.6	4.29 ± 0.04
^{244}Pu	^{244}Am	19 464 ± 27 [b]	0^+ (IAS)		~4.5

[a]) Excitation energies from the literature unless noted otherwise. [$A = 90$; ref. [51])], [$A = 117$; ref. [52])], [$A = 120$; ref. [53])], [$A = 208$; ref. [54])].

[b]) Present work.

[c]) Cross sections measured with a circular aperture centered at 0° with $\Delta\Omega = 3.43$ msr. The average angle is $\theta \approx 1.4°$ assuming a flat angular distribution.

[d]) Cross sections measured with a slit aperture centerd at 1° with $\Delta\Omega = 1.90$ msr. The average angle is $\theta \approx 1.6°$ assuming a flat angular distribution.

[e]) Ref. [10]). [f]) Ref. [34]).

4.1.4. $^{19}F(^3He, t)^{19}Ne$. Spectra at $E(^3\text{He}) = 200$ MeV were obtained with natural ThF_4 and UF_4 targets. They are dominated (not shown)by the strong mirror transitions to the $\frac{1}{2}^+$ ground state in ^{19}Ne, an IAS.

4.1.5. $^{28}Si(^3He, t)^{28}P$. The spectra for ^{28}Si obtained at $E(^3\text{He}) = 76.5$ MeV and 200 MeV (see figs. 4c, 5c and 6b) shows numerous states which were useful for energy calibration. The transition to the 1^+ state at 2.143 MeV in ^{28}P is the strongest at both bombarding energies.

4.1.6. $^{29,30}Si(^3He, t)^{29,30}P$. The isotopic abundances of 4.7% (^{29}Si) and 3.1% (^{30}Si) in natural silicon and the more positive Q-values lead to the observation of states in ^{29,30}P (fig. 5c). An expanded spectrum is shown in fig. 6c. Two strong transitions

TABLE 3

Experimental excitation energies E_x and Q-values or (^{3}He, t) transitions to isobaric analog states; experimental and calculated Coulomb displacement energies ΔE_{Coul}

Target nucleus	Final nucleus	E_x (keV) [a]	J^π	Q (keV)		ΔE_{Coul} (keV)			
						exp.		calc.	
				[a]	[b]	[a]	[d,e,f,g]	[h]	[i]
^{90}Zr	^{90}Nb	5072 ± 25	0^+	−11 202 ± 26	A	11 966 ± 26	11 999 ± 32 [g]	11 914	11 941
^{117}Sn	^{117}Sb	11 254 ± 60	$\frac{1}{2}^+$	−13 028 ± 60	A	13 792 ± 60	13 809 ± 16 [d]	13 815	13 827
^{120}Sn	^{120}Sb	10 247 ± 60	0^+	−12 946 ± 60	A	13 710 ± 60	13 667 ± 20 [d]	13 709	13 711
^{181}Ta	^{181}W	16 561 ± 15	$\frac{7}{2}^+$	−16 766 ± 15	B	17 530 ± 15	17 542 ± 6 [f]	17 578	17 495
^{nat}W	^{nat}Re			−16 904 ± 16 [c]	A	17 668 ± 16 [c]		17 675	17 650
^{197}Au	^{197}Hg	17 162 ± 15	$\frac{3}{2}^+$	−17 780 ± 16	A	18 544 ± 16		18 520	18 493
^{208}Pb	^{208}Bi	15 171 ± 18	0^+	−18 068 ± 18	A	18 832 ± 18	18 825 ± 9 [d]	18 885	18 901
^{230}Th	^{230}Pa		0^+	−19 044 ± 41	A				
			0^+	−19 110 ± 10	B				
			0^+	−19 079 ± 9	C				
		17 763 ± 18	0^+	−19 092 ± 17	ave	19 856 ± 17		19 887	19 838
^{232}Th	^{232}Pa		0^+	−19 015 ± 22	A				
			0^+	−19 027 ± 6	B				
			0^+	−19 029 ± 9	C				
		18 528 ± 11	0^+	−19 027 ± 5	ave	19 791 ± 5	19 743 ± 22 [e]	19 823	19 784
^{234}U	^{234}Np		0^+	−19 428 ± 22	A				
			0^+	−19 439 ± 8	B				
			0^+	−19 437 ± 14	C				
		17 608 ± 12	0^+	−19 438 ± 7	ave	20 202 ± 7		20 183	20 188
^{236}U	^{236}Np		0^+	−19 388 ± 40	B				
			0^+	−19 376 ± 33	C				
		18 433 ± 57	0^+	−19 381 ± 26	ave	20 145 ± 26		20 107	20 140
^{238}U	^{238}Np		0^+	−19 275 ± 18	A				
			0^+	−19 285 ± 6	B				
			0^+	−19 271 ± 9	C				
		19 115 ± 8	0^+	−19 280 ± 7	ave	20 044 ± 7	20 019 ± 40 [e]	20 058	20 092
^{244}Pu	^{244}Am	19 464 ± 27	0^+	−19 558 ± 27	A	20 322 ± 27		20 274	20 427

[a] Present work.
[b] A = 200 MeV singles; B = 76.5 MeV singles; C = 76.5 MeV coincidences; ave = average
[c] Centroid value for $A = 184$.
[d] Ref. [34]). [e] Ref. [4]). [f] Ref. [10]). [g] Ref. [55]). [h] Ref. [18]). [i] Ref. [19]).

are observed for states in ^{29}P. These are the mirror transition to the $\frac{1}{2}^+$ ground state, an IAS, and the transition to the $\frac{1}{2}^+$ state at 4.760 MeV. Three strong transitions are observed for states in ^{30}P. These are two Gamow–Teller transitions to the 1^+ ground state and state at 3.019 MeV, and the transition to the 0^+ IAS at 0.677 MeV. As expected, the two analog-state transitions have nearly equal Q-values but separate cross sections could be extracted by unfolding the slightly broadened line.

4.1.7. ^{90}Zr(^{3}He, t)^{90}Nb. The transition to the 0^+ IAS at 5.072 MeV in ^{90}Nb dominates the spectrum obtained at $E(^3\text{He}) = 200$ MeV (see fig. 7a). Several low-lying states are also observed, particularly the 1^+ state at 2.126 MeV. Broad structures from Gamow–Teller and electric giant resonances centered near 9 MeV and 19 MeV are also seen but become more clearly visible with expanded vertical scales (not shown). As mentioned before, the spectrum displays a strong peak from

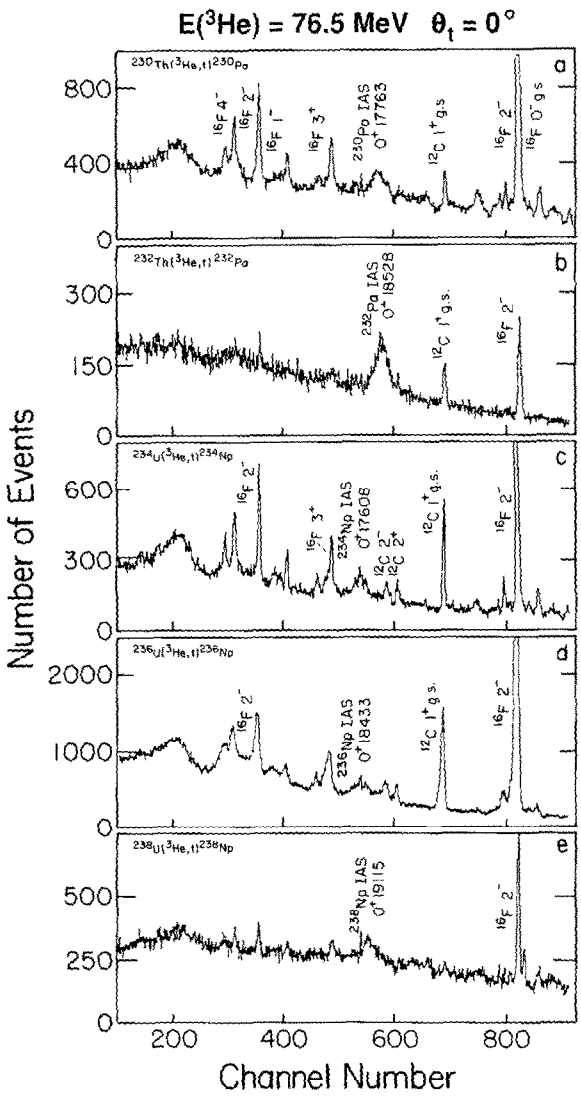

Fig. 11. Triton energy spectra from the (^{3}He, t) reaction obtained with the QMG/2 magnetic spectrograph (KVI) at $E(^3\text{He}) = 76.5$ MeV, $\theta_t = 0°$ and identical magnetic field settings for targets of $^{230}ThO_2$ on (a) Al, (b) ^{nat}Th, (c) ^{234}U acetate on Al, (d) ^{236}U acetate on Al, (e) $^{nat}UF_4$ on Al. Excitation energies are given in keV.

singly-ionized $^3He^+$ particles due to atomic charge exchange in the target material. This line was blocked out for most other spectra.

4.1.8. $^{117}Sn(^3He, t)^{117}Sb$. The transition to the $\frac{1}{2}^+$ IAS at 11.271 MeV in ^{117}Sb dominates the spectrum observed at $E(^3\text{He}) = 200$ MeV (not shown). The spectrum is similar to that for the ^{120}Sn target (fig. 7b) and includes a few transitions to low-lying states and broad structures centered near 13 MeV and 22 MeV.

4.1.9. ^{120}Sn(^{3}He, t)^{120}Sb. The transition to the 0^+ IAS at 10.204 MeV in ^{120}Sb dominates the spectrum obtained at $E(^3\text{He}) = 200$ MeV (see fig. 7b). An angular distribution for this state has been measured and is discussed in sect. 4.2. Furthermore, a few low-lying states up to about 2 MeV are weakly excited, as are broad structures centered near 12 MeV and 21 MeV.

4.1.10. ^{181}Ta(^{3}He, t)^{181}W. The transition to the IAS at 16.573 MeV in ^{181}W was observed at $E(^3\text{He}) = 76.5$ MeV with the Ta_2O_3 target (fig. 4b).

4.1.11. ^{197}Au(^{3}He, t)^{197}Hg. The transition to the IAS predicted at $E_x =$ 17.162 MeV in ^{197}Hg was observed at $E(^3\text{He}) = 200$ MeV from the Au backing of the WO_3 target (see fig. 5b).

4.1.12. ^{nat}W(^{3}He, t)Re. The transitions to the unresolved group of IAS predicted near 15.450 MeV in the four final rhenium isotopes was observed at $E(^3\text{He}) =$ 200 MeV with the WO_3 target (see fig. 5b). The centroid energy of the broadened line can be used to extract a Q-value for the most abundant isotope with $A = 184$.

4.1.13. ^{208}Pb(^{3}He, t)^{208}Bi. The transition to the 0^+ IAS at 15.165 MeV in ^{208}Bi dominates the spectrum observed at $E(^3\text{He}) = 200$ MeV (see fig. 8a). In addition, about 12 low-lying states are observed up to excitation energies of 5 MeV as is a broader resonance at 5.6 MeV. Several of these states have pronounced 0° maxima seen clearly by raytracing. Also observed are broad resonances centered near 16 MeV and 24 MeV. An expanded spectrum, fig. 10a, shows the finite width of the IAS and the lorentzian line shape.

4.2. ANGULAR DISTRIBUTIONS

An angular distribution from 0° to 16° for the transition to the IAS in the reaction ^{120}Sn(^{3}He, t)^{120}Sb (fig. 7b) was obtained at $E(^3\text{He}) = 200$ MeV with an angle resolution of $\Delta\theta \approx 1°$. It is displayed in fig. 12. The two data points near zero degrees were extracted by ray tracing from the zero-degree measurement with a rectangular aperture. The measured distribution displays a very pronounced oscillatory structure. Also shown in the figure is a calculated distribution (see subsect. 5.3).

4.3. (^{3}He, t) AND (^{3}He, tp) ON ACTINIDE TARGETS

Measurements were made at $E(^3\text{He}) = 200$ MeV on the target nuclei ^{230}Th, ^{232}Th, ^{234}U, ^{236}U, ^{238}U, ^{244}Pu (see table 1). The transition to the 0^+ IAS at 18.528 MeV in ^{232}Pa from the bombardment of the natural thorium foil, a relatively thick target, shows up very strongly (fig. 8b). Lines from oxygen contaminants are discernible but do not interfere. The spectra obtained with the natural ThF_4 and UF_4 targets on carbon backings also show the IAS quite well. An expanded spectrum from the region of the 0^+ IAS at 19.115 MeV in ^{238}Np is displayed in fig. 9a. It is superimposed on the ^{12}N spectrum generated by the carbon backing. This background spectrum has low intensity in the region of interest near $E_x = 2$ MeV in ^{12}N as can be seen from the comparison of figs. 9a and 9b. The IAS for the thin oxide targets of ^{230}Th, ^{234}U, ^{236}U and ^{244}Pu are only barely observable because of background from the

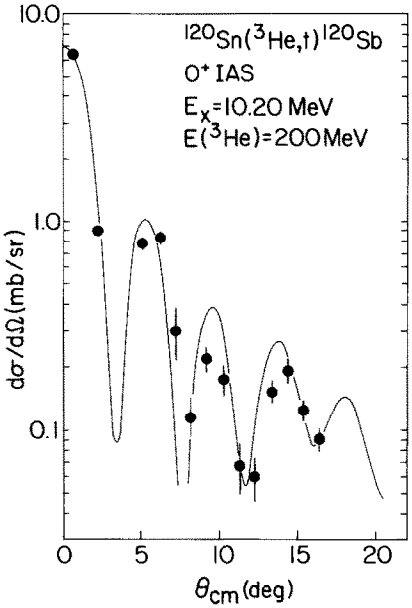

Fig. 12. Angular distribution for ^{120}Sn(^{3}He, t)^{120}Sb(IAS) measured at $E(^3\text{He}) = 200$ MeV and comparison with microscopic calculations.

carbon backings, but some information about Q-values and widths could nevertheless be extracted.

As mentioned in subsect. 4.1., corrected difference spectra for the actinide targets were generated by subtracting properly normalized carbon and/or oxygen spectra (e.g. spectrum fig. 9a minus spectrum fig. 9b). Results are displayed in fig. 10 including fits with lorentzian line shapes for the respective IAS. Fluctuations in the regions of the subtracted contaminant lines are marked by arrows. They are due to differing energy resolution, primarily from target thickness. The cross sections, Q-values, excitation energies and total widths Γ extracted from the 200 MeV data are included in tables 2, 3 and 4. The latter were corrected for the finite experimental energy resolution.

Measurements were made at $E(^3\text{He}) = 76.5$ MeV on oxide, fluoride or acetate targets of ^{230}Th, ^{232}Th, ^{234}U, ^{236}U and ^{238}U on aluminium backings (see table 1). This included coincidence measurements with decay protons, which allows the extraction of branching ratios and partial decay widths.

The spectra obtained from the bombardment of the various actinide targets show the 0^+ IAS in ^{230}Pa, ^{232}Pa, ^{234}Np, ^{236}Np and ^{238}Np quite clearly at excitation energies near 18 MeV. Some interference from reactions on ^{12}C, ^{16}O and also ^{27}Al is present, though. The uncorrected spectra are displayed in fig. 11.

An example for a two-dimensional display of proton energy E_p versus triton energy E_t for the coincidence experiment is shown in fig. 3. The proton decay

TABLE 4

Branching ratio for proton decay and experimental and calculated total, escape and spreading widths

Target nucleus	Final nucleus	Exp [a]	$P^\uparrow$ (%)	Present work			Known [b,c]		Calc. [d]	
				Γ (keV)	$\Gamma^\uparrow$ (keV)	$\Gamma^\downarrow$ (keV)	Γ (keV)	$\Gamma^\downarrow$ (keV)	$\Gamma^\downarrow$ (keV) $\beta = 0$	$\Gamma^\downarrow$ (keV) $\beta \neq 0$
^{208}Pb	^{208}Bi	A		230 ± 17			232 ± 6	78 ± 8	53	69
^{230}Th	^{230}Pa	B		217 ± 15						
		C		203 ± 16						
		ave	56 ± 6	210 ± 11	118 ± 14	92 ± 14			65	121
^{232}Th	^{232}Pa	A		280 ± 14						
		B		271 ± 14						
		C		258 ± 15						
		ave	45 ± 3	270 ± 9	122 ± 9	148 ± 10	306 ± 20	90 ± 20	66	127
^{234}U	^{234}Np	A		193 ± 60						
		B		262 ± 25						
		C		268 ± 22						
		ave	54 ± 6	261 ± 19	141 ± 19	120 ± 18			67	135
^{236}U	^{236}Np	B		233 ± 50						
		C		246 ± 24						
		ave	60 ± 13	243 ± 22	146 ± 34	97 ± 33			68	140
^{238}U	^{238}Np	A		346 ± 17						
		B		352 ± 19						
		C		311 ± 29						
		ave	48 ± 4	343 ± 14	165 ± 16	178 ± 16	380 ± 40	142 ± 37	69	145
^{224}Pu	^{244}Am	A		337 ± 90					73	161

[a] Notation as in table 3.
[b] Ref. [4]. [c] Ref. [56]. [d] Ref. [20].

energies increase with increasing excitation energies, and a pronounced correlation therefore exists between the two energies. This can be seen from the reactions on the contaminant nuclei ^{27}Al, ^{16}O and ^{12}C leading to proton-unstable states and resonances which decay into discrete ground or excited final states. The proton-decay energies for the IAS in the actinide nuclei are considerably higher than those for the contaminants, and rather clean triton spectra can therefore be projected out. The results are shown in fig. 13.

Fig. 14 displays for Q-values from -21 to -18 MeV corrected triton spectra without and with the requirement of a proton coincidence. The corrected singles spectra were again obtained by subtracting properly normalized spectra obtained for carbon and oxygen targets (figs. 4a and 4b). The IAS are clearly observed, particularly for the coincidence data. Fig. 14 further includes fits to the background and to the IAS with lorentzian line shapes. The cross sections, Q-values, excitation energies and total widths Γ extracted from the 76.5 MeV data are included in tables 2, 3 and 4. The total widths are corrected for the finite experimental energy resolution. Also included in table 4 are the escape probabilities $P^\uparrow$ describing the probability of proton emission from the IAS. Assuming an isotropic distribution of the decay

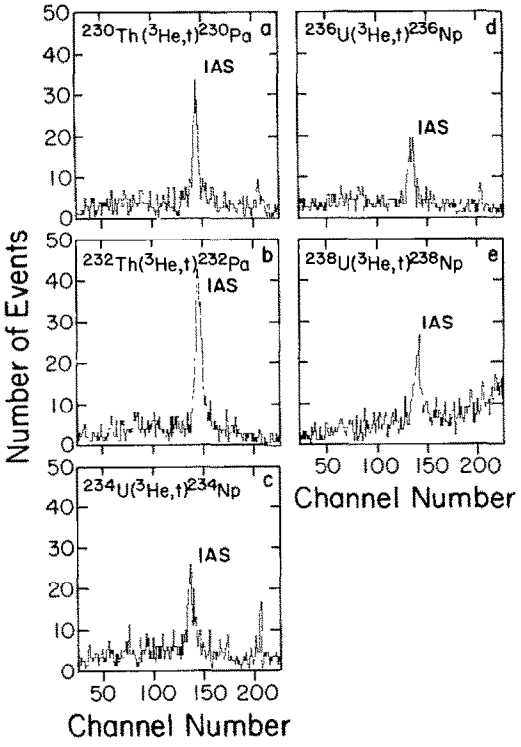

Fig. 13. Triton energy spectra from the (^{3}He, tp̄) reaction obtained for IAS of actinide targets in coincidence with decay protons (true = prompt minus random; see figs. 2 and 3) at $E(^3\mathrm{He}) = 76.5$ MeV, $\theta_t = 0°$ and identical magnetic field settings. The targets are those of fig. 11.

protons, $P^\uparrow$ is obtained from

$$P^\uparrow = 4\pi \frac{\mathrm{d}^2\sigma\,(\theta_t = 0°;\, \theta_p)/\mathrm{d}\Omega_t\,\mathrm{d}\Omega_p}{\mathrm{d}\sigma(\theta_t = 0°)/\mathrm{d}\Omega_t} \qquad (1)$$

where the double-differential cross section $\mathrm{d}^2\sigma/\mathrm{d}\Omega_t\,\mathrm{d}\Omega_p$ is the cross section derived from fig. 13 for the (^{3}He, t) reaction to the IAS with the simultaneous observation of decay protons. Combining the total widths Γ and escape probabilities $P^\uparrow$ makes it possible to extract escape widths $\Gamma^\uparrow$ and spreading widths $\Gamma^\downarrow$ (see table 4 and subsect. 5.2).

5. Discussion

5.1. COULOMB DISPLACEMENT ENERGIES OF ACTINIDE NUCLEI

The experimental Q-values for the transitions to IAS and the respective excitation energies are listed in columns 5 and 3 of table 3. The Q-values were used to deduce Coulomb displacement energies ΔE_{Coul} (column 7) from the equation $\Delta E_{\mathrm{Coul}} = -Q + \Delta E_{\mathrm{Coul}}(^3\mathrm{He}\text{-}^3\mathrm{H})$ with $\Delta E_{\mathrm{Coul}}(^3\mathrm{He}\text{-}^3\mathrm{H}) = 763.8$ keV. A comparison with known

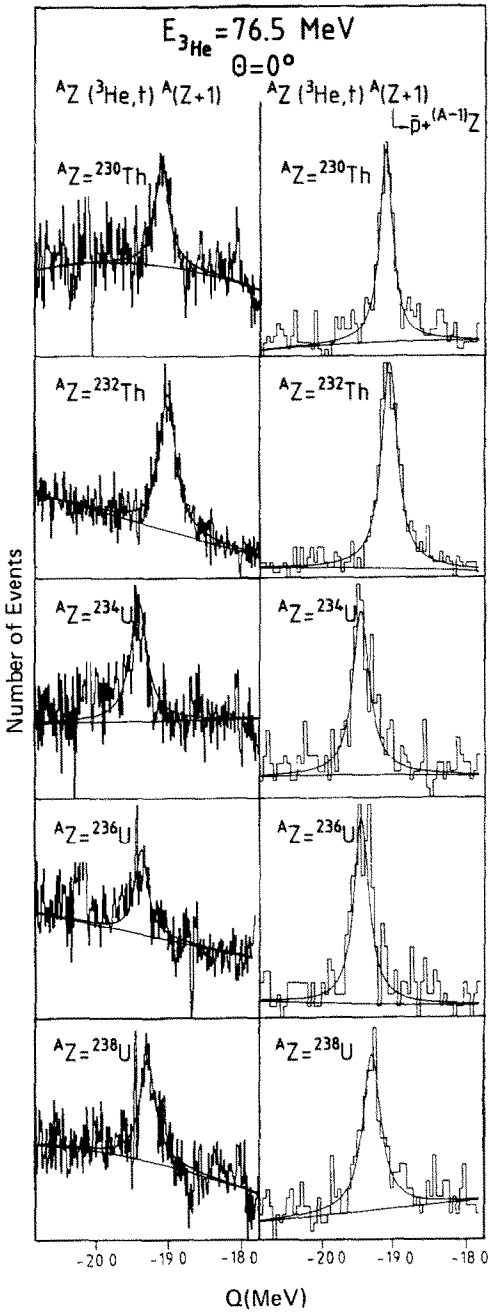

Fig. 14. Triton energy spectra from (^{3}He, t) and (^{3}He, tp̄) corrected for background obtained for IAS of actinide targets in singles and in coincidence mode at $E(^3\mathrm{He}) = 76.5$ MeV, $\theta_t = 0°$ with lorentzian line shape fitting.

energies (column 8) shows good agreement. New values for displacement energies are reported for the parent nuclei ^{184}W, ^{187}Au, ^{230}Th, ^{234}U, ^{236}U and ^{244}Pu, and revised values with significantly reduced uncertainties are reported for ^{232}Th and ^{238}U. These results greatly improve our knowledge of Coulomb displacement energies for nuclei heavier than ^{208}Pb.

Numerous equations have been derived to estimate Coulomb energies and Coulomb displacement energies of atomic nuclei beginning with the liquid-drop-model expression of Bethe and Weizsäcker [31,32]). It was soon modified to include the quantum-mechanical exchange term which arises from the antisymmetrization of the wave function [32,33]). The liquid drop model and the shell model are most commonly used to estimate Coulomb displacement energies, and table 3 (columns 9 and 10) includes the results from recently derived shell-model equations [18,19]). These equations describe nuclear Coulomb energies in terms of the Coulomb interactions between individual protons in the same or in different shell-model orbits, whereas A-dependent size factors account for the effect of the increase in charge radius. Deformation effects are explicitly included in the equations of ref. [18]), and implicitly in those of ref. [19]). The most recent data base, including the data from the present work, was used for the calculations shown in column 10. Both sets of predictions agree well with the new data.

A direct estimate of the change in electrostatic energies due to the deformation of the nuclear shape can be obtained by comparing the experimental results to predictions for spherical nuclei. The simple procedure is essentially that employed for the deformed rare-earth nuclei [5]). Here, the equation

$$\Delta E_{\mathrm{Coul}} = a\frac{Z_< + 0.5}{A^{1/3}} - b \tag{2}$$

is assumed to describe ΔE_{Coul} for spherical nuclei. The two terms in the equation represent essentially the direct liquid-drop energy and, assuming $(Z/A)^{1/3} \approx$ constant, the exchange energy. The two parameters a and b were determined from a fit with $\sigma \approx 20$ keV to data [compiled in ref. [34])] for 16 spherical nuclei with $N = 82 \pm 1$ and $Z = 82 \pm 1$ ($a = 1377.4$ keV, $b = 352.5$ keV). Fig. 15 displays the differences between experimental and calculated Coulomb displacement energies for the nuclei with $Z \geq 81$ including the present actinide nuclei. The energies for the actinide nuclei are reduced by about 150 keV, an effect quite similar to that observed in the rare-earth region [5]) where a reduction of about 120 keV is observed for the strongly deformed nuclei.

The influence of quadrupole and hexadecapole deformations on ΔE_{Coul} can be estimated with a correction factor $1 - C(\beta_2, \beta_4)$ leading to

$$\Delta E^{\mathrm{def}}_{\mathrm{Coul}} - \Delta E^{\mathrm{sph}}_{\mathrm{Coul}} = -C(\beta_2, \beta_4)\Delta E^{\mathrm{sph}}_{\mathrm{Coul}}. \tag{3}$$

In lowest order $C(\beta_2, 0) = \beta_2^2/4\pi$. An expression including the effect of β_4 and higher orders in β_2 is [35])

$$C(\beta_2, \beta_4) = B_2^2 + \tfrac{4}{21}\sqrt{5}B_2^3 - \tfrac{255}{49}B_2^4 + \tfrac{18}{7}B_2^2B_4 + \tfrac{5}{3}B_4^2 \tag{4}$$

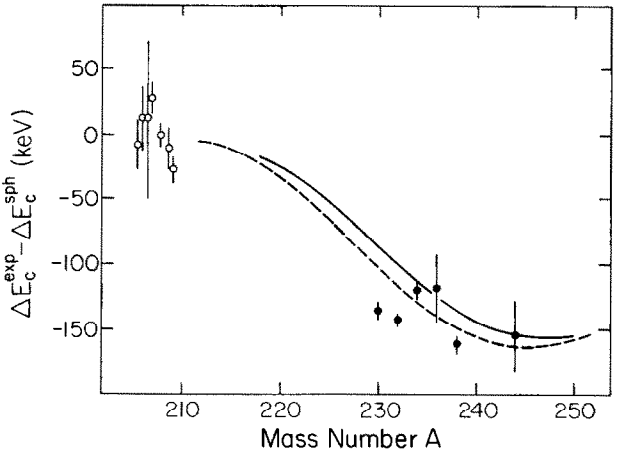

Fig. 15. Difference of Coulomb displacement energies for deformed and spherical nuclei as function of mass number A. The calculated curves make use of eqs. (2) and (3) with deformation parametes β_2 and β_4 calculated for nuclei along the line of beta stability (see text). The solid curve includes the effect of β_2 whereas the dashed curve includes also the effect of hexadecapole deformation β_4.

with $B_2 = \beta_2/(4\pi)^{1/2}$ and $B_4 = \beta_4/(4\pi)^{1/2}$. Fig. 15 includes calculated energy differences based on eqs. (2) and (3) for nuclei along the line of β-stability approximated by $(N-126) = 2(Z-82)$. Here, the deformation parameters β_2 and β_4 were described by a simple parameterization [36])

$$\beta_2 = \alpha_1 f(x, y) + \alpha_2 , \tag{5}$$

$$\beta_4 = \alpha_3 (z_0 - z) f(x, y) , \tag{6}$$

$$f(x, y) = x(1-x)(2-x)y(1-y)(2-y) , \tag{7}$$

with $x = (Z-82)/32$, $y = (N-126)/58$, $z = x + y$. The parameters were extracted using recent data [37]) for β_2 and β_4 ($\alpha_1 = 1.7754$, $\alpha_2 = 0.050$, $\alpha_3 = 1.43$, $z_0 = 0.94$).

The results shown in fig. 15 confirm the influence of the deformation of the nuclear shape on Coulomb displacement energies. The agreement between experimental and calculated values must be considered as very good considering the simplicity of the calculations. The hexadecapole deformation β_4 contributes at most 15 keV to the reduction in Coulomb displacement energies. The slight underestimation of the effect for ^{230}Th and ^{232}Th may be related to a similar observation for the low-A rare-earth data [5]) which is not yet understood.

5.2. TOTAL WIDTHS Γ, ESCAPE WIDTHS $\Gamma^\uparrow$, AND SPREADING WIDTHS $\Gamma^\downarrow$ OF ISOBARIC ANALOG STATES OF ACTINIDE NUCLEI

Isobaric analog states can be constructed by applying the isospin-lowering operator T_- to the ground-state wave functions of the parent nuclei. They have

therefore a simple nuclear structure, and the coherent superposition of particle-hole excitations essentially preserves the simplicity of the ground-state wave function of the parent nucleus including its isospin $T_0 = \frac{1}{2}|(N-Z)|$. However, admixtures of lower isospin are ususally present,

$$|\mathrm{IAS}\rangle = \alpha_{T_0}|T_0\rangle + \alpha_{T_0-1}|T_0-1\rangle\,, \tag{8}$$

due to Coulomb and other isospin-violating charge-dependent interactions which lead to isospin mixing with certain underlying states of lower isospin. The quantity $(\alpha_{T_0-1})^2$ is typically of the order of a few percent.

Most IAS are unstable with regard to particle emission, and the total width Γ can, according to eq. (8), be written as

$$\Gamma = \Gamma^{\uparrow} + \Gamma^{\downarrow}\,. \tag{9}$$

Here, $\Gamma^{\uparrow}$ is the escape width associated with isospin-allowed proton decay from the main component of the IAS. Isospin-allowed neutron decay becomes energetically possible only through the admixtures of lower isospin in the wave function, and it is therefore associated with the spreading with $\Gamma^{\downarrow}$. Neutron decay is not hindered by a Coulomb barrier, and the two decay modes are usually comparable. There are even a few instances when neutron decay dominates. Fission decay contributes typically 25% to $\Gamma^{\downarrow}$ in heavier nuclei [4]).

Proton decay leads to transitions to discrete low-lying single-neutron-hole states. The escape width $\Gamma^{\uparrow}$ is therefore a sensitive function of (i) the proton separation energy S_p, (ii) the height of the Coulomb barrier, and (iii) the nuclear structure of both the IAS and the single-neutron hole states in the daughter nucleus. The latter affects the decay probability via the angular momentum l and a spectroscopic strength factor. A quantitative procedure has been established recently [21]) which makes it possible to relate the contributions to $\Gamma^{\uparrow}$ to the spectroscopic factors of single-neutron pickup reactions on the target nucleus. The dependence of $\Gamma^{\uparrow}$ on S_p is responsible for a pronounced odd-A/even-A staggering effect observed earlier for the total width Γ of the IAS of Sn isotopes [3]). Here, $\Gamma^{\uparrow}$ contributes about 30% to the total width Γ in the odd-A isotopes but only an estimated [3]) <5 keV in the even-A isotopes. This latter estimate is confirmed by a calculation [21]) based on the experimental spectroscopic factors of ^{122}Sn(p, d)^{121}Sn leading to $\Gamma^{\uparrow} \approx 5$ keV. The escape widths $\Gamma^{\uparrow}$ for the IAS of even-even nuclei increase with increasing mass number A from $\sim$5 keV for the Sn isotopes to values ranging from 6 to 35 keV for the Nd isotopes [9]) to about 150 keV for ^{208}Pb [ref. [21])]. Except for the high value for ^{208}Pb, this general trend continues with $\Gamma^{\uparrow} \approx 140$ keV for the actinide nuclei observed in the present work (see table 4). Escape widths also seem to increase with increasing neutron excess [9]).

The spreading width $\Gamma^{\downarrow}$ of IAS represents a measure of their isospin purity. Configuration or anti-analog states contribute to $\Gamma^{\downarrow}$ in light nuclei, but in heavier

nuclei with $A > 100$ it is believed that $\Gamma^{\downarrow}$ is primarily the result of isospin mixing due to coupling to more complicated states of lower isospin $T_< = T_0 - 1$ mediated by coupling via the Coulomb force to the $(T_0 - 1)$-component of the isovector giant monopole resonance (IVGMR) [38,39]) which thus acts as a doorway state. This leads to a generally smooth increase of $\Gamma^{\downarrow}$ with mass number. A recent global analysis [20]) of the experimental spreading widths $\Gamma^{\downarrow}$ of 65 IAS from $A = 110$ to 238 has resulted in excellent agreement with the data over the entire range and has established smooth trends for the parameters describing the IVGMR. Here, a strength-function approach [40]) for the damping widths of IVGMR resonances was successfully employed. However, it became necessary to introduce an explicit dependence on nuclear deformation to account for the increase of the observed spreading widths with neutron exess in several sequences of deformed rare-earth isotopes [9,5]). A splitting of the IVGMR strength in deformed nuclei due to coupling to the beta-vibration component of the isovector giant quadrupole resonance (IVGQR) had to be postulated similar to the observed behavior for isoscalar resonances. It was represented by an additional linear dependence on the deformation of the A-dependent second moment of the strength function of the IVGMR, and the strong increase in spreading width with neutron excess could indeed be explained [20]).

The global increase of the experimental spreading widths $\Gamma^{\downarrow}$ with increasing neutron excess can also be described [22]) quite well with a phenomenological expression. Here use is made of a constant second moment of the strength function of the IVGMR.

The spreading width $\Gamma^{\downarrow}$ can be determined experimentally by observing the statistical neutron decay [and/or fission decay; see ref. [4])] from an IAS directly and by measuring both the total width Γ and the branching ratio $P^{\downarrow}$ for neutron emission. One can also measure the semi-direct proton decay from an IAS and determine, for example, the double differential cross section for the detection of tritons populating the IAS in the (^{3}He, t) reaction in coincidence with decay protons. The escape probability $P^{\uparrow}$ is then obtained from eq. (1), and the escape and spreading widths can be determined from

$$\Gamma^{\uparrow} = P^{\uparrow}\Gamma, \tag{10}$$

$$\Gamma^{\downarrow} = (1 - P^{\uparrow})\Gamma. \tag{11}$$

This latter procedure was employed in the present work. The data reduction is described in subsect. 4.3, and the results for $P^{\uparrow}$, Γ, $\Gamma^{\uparrow}$ and $\Gamma^{\downarrow}$ are included in table 4.

Fig. 16 displays the measured total and spreading widths for the IAS of ^{208}Pb and the six actinide nuclei as function of mass number. The earlier values for the total widths Γ of the IAS in ^{208}Bi, ^{232}Pa and ^{238}Np are in good agreement with the new data. The spreading widths $\Gamma^{\downarrow}$ of the IAS in ^{232}Pa and ^{238}Np determined from

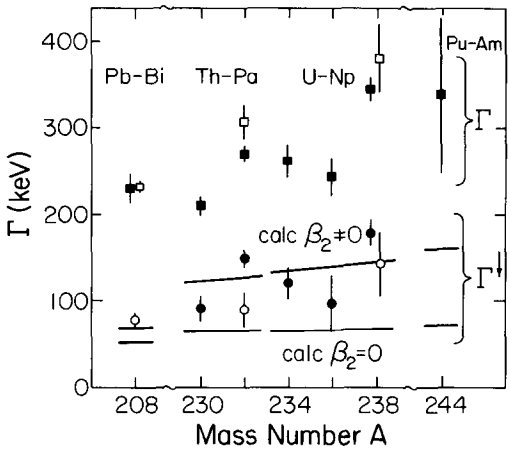

Fig. 16. Total width Γ and spreading widths $\Gamma^{\downarrow}$ for actinide nuclei from the present work (closed squares and circles), comparison with known values (open squares and circles), and comparison with predictions with and without the inclusion of deformation-dependent effects (see text).

the fission decay of the isobaric analog states [4]) also agree reasonably well with the new data except for $\Gamma^{\downarrow}$ of ^{232}Pa which is slightly low. There is a general trend for all widths, Γ, $\Gamma^{\uparrow}$ and $\Gamma^{\downarrow}$, to increase with increasing mass number A starting from ^{208}Pb. The comparison with the spreading widths calculated [20]) on the basis of isospin mixing with the $T_<$-component of the IVGMR shows all data points higher than those predicted without the inclusion of the postulated splitting of the IVGMR strength in deformed nuclei. The agreement is improved when IVGMR splitting due to the nuclear deformation is taken into account. This supports the earlier analysis despite the fact that the data points display some fluctuations. The data are also essentially in agreement with the trend provided by a phenomenological dependence on neutron excess [22]).

5.3. THE EFFECTIVE NON-SPIN-FLIP INTERACTION V_τ AT $E(^3\text{He}) \approx 75$ MeV AND 200 MeV

An effective ^{3}He-nucleon interaction appropriate for a microscopic one-step DWBA (distorted wave Born approximation) analysis of the (^{3}He, t) charge-exchange reaction has been established [11]) for energies in the range $E(^3\text{He}) = 65$ to 90 MeV [see also refs. [14–16])],

$$V_{\text{eff}} = \{V_\tau \cdot Y(r/R_c) + V_{\sigma\tau}(\boldsymbol{\sigma}_1 \cdot \boldsymbol{\sigma}_2) \cdot Y(r/R_c) + V_{T\tau} \cdot r^2 \cdot S_{12} \cdot Y(r/R_{T\tau})\} \cdot (\boldsymbol{\tau}_1 \cdot \boldsymbol{\tau}_2) . \quad (12)$$

Here, the quantities V_τ, $V_{\sigma\tau}$, and $V_{T\tau}$ parameterized with single Yukawa potentials

TABLE 5

Amplitudes for particle/hole excitations for transitions to IAS

$^{30}Si \rightarrow {}^{30}P$

$0.1108\,(d_{5/2}^{-1}, d_{5/2}) + 0.4186\,(s_{1/2}^{-1}, s_{1/2}) + 0.2753\,(d_{3/2}^{-1}, d_{3/2})$

$^{90}Zr \rightarrow {}^{90}Nb$

$1.0000\,(g_{9/2}^{-1}, g_{9/2})$

$^{120}Sn \rightarrow {}^{120}Sb$

$0.214\,(s_{1/2}^{-1}, s_{1/2}) + 0.316\,(d_{3/2}^{-1}, d_{3/2}) + 0.531\,(d_{5/2}^{-1}, d_{5/2}) + 0.600\,(g_{7/2}^{-1}, g_{7/2}) + 0.502\,(h_{11/2}^{-1}, h_{11/2})$

$^{208}Pb \rightarrow {}^{208}Bi$

$0.2132\,(p_{1/2}^{-1}, p_{1/2}) + 0.3015\,(p_{3/2}^{-1}, p_{3/2}) + 0.3693\,(f_{5/2}^{-1}, f_{5/2}) + 0.4264\,(f_{7/2,7/2}^{-1}) + 0.5641\,(i_{13/2}^{-1}, i_{13/2})$
$+ 0.4761\,(h_{9/2}^{-1}, h_{9/2})$

were deduced from angular distributions for transitions to selected states. This effective interaction applies to the present 76.5 MeV data, but its applicability to the 200 MeV data is untested. Energy-dependent interaction strengths may require adjustments. The present work concentrates on the interaction V_τ which is responsible for transitions to IAS. Although the interaction $V_{LS\tau}$ must in principle also be considered in transitions to natural-parity states, its contributions in (^{3}He, t) reactions is not well understood. It was observed at lower bombarding energies [11]) that even small admixtures caused a deterioration of the fits for transitions to IAS, and this term will therefore be neglected in the analysis of the 200 MeV data.

The experimental angular distribution of fig. 12 for ^{120}Sn(^{3}He, t)^{120}Sb(IAS) allows the most direct comparison with calculated predictions. Here, a microscopic description was used for the form factor. The amplitudes for particle/hole excitations were determined from $c_{pH} \propto [(2j+1)v_j^2]^{1/2}$ where v_j are the occupation numbers obtained from BCS wave functions. These amplitudes are included in table 5. The ^{3}He optical model parameters are those extracted [41]) at $E(^3\text{He}) = 217$ MeV. They are included in table 6. As discussed earlier [11]) the triton optical model parameters were obtained by scaling the well depths of the ^{3}He parameters by a factor of 0.85. The Yukawa

TABLE 6

^{3}He optical-model parameters

Nucleus	V_0 (MeV)	W_0 (MeV)	r_V (fm)	r_W (fm)	a_V (fm)	a_W (fm)	r_C (fm)
^{28}Si	−84.5	−23.7	1.14	1.46	0.86	0.73	1.30
^{90}Zr	−76.2	−26.1	1.24	1.39	0.83	0.79	1.30
^{120}Sn	−70.9	−28.9	1.27	1.40	0.86	0.69	1.30
^{208}Pb	−78.0	−24.1	1.25	1.43	0.86	0.81	1.30

shape of the effective interaction was identical to that used earlier [11]) with a range of $R_\tau = 1.415$ fm deduced from a folding calculation [14]). The DWBA calculations were performed with the code DW81 [42]) using only the quantity V_τ as adjustable parameter. The calculated angular distribution is included in fig. 12. Its shape shows excellent agreement with the measured distribution. The effective interaction energy was adjusted and found to be $V_\tau = 3.47$ MeV. It is included in table 7 together with other interaction energies.

More limited data of zero-degree cross sections were used to obtain values of V_τ for the transitions to IAS in ^{30}P, ^{90}Nb and ^{208}Bi. The transition amplitudes used for the calculations are included in table 5. The values for the ^{30}Si target are based on Brown-Wildenthal wave functions [43]). A simple $(g_{9/2}^{-1}, g_{9/2})$ contribution was assumed for ^{90}Zr. For ^{208}Pb the contributions are obtained by operating with the T_- operator on an assumed closed-shell configuration for ^{208}Pb. The respective optical-model parameters are included in table 6. The parameters for ^{28}Si were used in the ^{30}Si calculations, and all triton parameters were again scaled as mentioned before [11]). In comparing the experimental cross sections of tables 2a and 2b with the calculations, the calculated cross sections were averaged over an angular range near zero degrees consistent with that subtended by the respective apertures which were different for the runs with ^{120}Sn and ^{208}Pb from those with ^{30}Si and ^{90}Zr. Effective interaction strengths V_τ were again extracted, and the results are included in table 7.

Table 7 displays the effective interaction strengths V_τ extracted earlier at energies $E(^3\text{He})$ from 65 to 90 MeV (or 22 to 30 MeV/u), and the values determined in the

TABLE 7

Effective interaction strength V_τ determined from transitions to IAS

Nucleus	E_x (MeV)	$E(^3\text{He})$ (MeV)	V_τ [a]) (MeV)	Configuration
^{26}Al	0.228	73	6.93	Brown-Wildenthal [43])
^{42}Sc	0.000	73	6.50	Brown-Wildenthal [43])
^{48}Sc	6.67	66	7.25	Brown-Wildenthal [43])
^{58}Cu	0.203	73	6.50	Brown-Wildenthal [43])
^{90}Nb	5.072	89.3	5.70	$(g_{9/2}^{-1}, g_{9/2})$
			6.60	
^{30}P	0.677	200	3.09	see table 5
^{90}Nb	5.072	200	3.95	see table 5
^{120}Sb	10.204	200	3.47	see table 5
^{208}Bi	15.165	200	5.40	see table 5
			3.98	

[a]) Results for $E(^3\text{He}) < 100$ MeV from ref. [11]).
Results for $E(^3\text{He}) = 200$ MeV from present work.

present work at $E(^3\text{He}) = 200$ MeV (or 67 MeV/u). The averaged values show a distinct decrease from 6.60 MeV to 3.98 MeV. This decrease by a factor 0.6 is in good agreement with the decrease observed for V_τ in the (p, n) reaction [44]) in the range of 25 to 45 MeV incident energy combined with the observed increase in the ratio $V_{\sigma\tau}/V_\tau$ over a wider energy range [44]) and the fact that $V_{\sigma\tau}$ is expected [45]) to vary very slowly for these energies. This comparison supports the close relationship between (p, n) and (^{3}He, t) charge-exchange reactions.

5.4. OTHER DISCRETE STATES

In addition to the IAS, numerous discrete states and broad resonances have been observed in the present experiment. Only a few remarks will be made about these.

The cross sections for the Fermi and Gamow-Teller transitions to the two strongly excited states in ^{13}N (fig. 6a) are approximately equal. The comparison of these cross sections [17,45]) leads to the conclusion that non-spin-flip and spin-flip transitions are about equal in strength for (^{3}He, t) at $E(^3\text{He}) = 200$ MeV.

Numerous additional spin-flip Gamow-Teller transitions have been observed in the present work to low-excited 1^+ states in many nuclei (see figs. 4a, 5a, 5c, 6b, 7a, 7b, 8a). Such states are usually difficult to observe in (p, n) charge-exchange reactions due to the much lower energy resolution. The advantage of charged-particle spectroscopy at $\theta_t = 0°$ is evident, but the interpretation of the observed cross sections may be more involved.

5.5. RESONANCES

Broad Gamow-Teller resonances as well as non-spin-flip electric giant dipole resonances have also been observed on several targets including ^{90}Zr, ^{117}Sn, ^{120}Sn, ^{208}Pb and ^{232}Th at excitation energies in the range from about 10 MeV to 20 MeV (see figs. 7a, 7b, 8a, 8b and tables 2a and 2b). The ray-tracing capability of the focal-plane detection system allows the simultaneous measurement of 0° and 2° cross sections. Unique identification of $L = 0$ and $L = 1$ transitions is therefore possible.

5.6. NON-RESONANT BACKGROUND

A continuous non-resonant background is apparent in all spectra with thresholds at the 3-body breakup energies. A preliminary analysis was performed for the ^{120}Sn target. Quasi-free charge exchange [see e.g. refs. [46,47])] was observed to be dominant up to effective excitation energies of 40 MeV. Above effective excitation energies of 40 MeV the (^{3}He, t$\bar{\text{p}}$) breakup/pickup reaction [48–50]) becomes experimentally very important, particularly at $\theta_t = 0°$ (not shown). A quantitative description of the non-resonant background appears possible.

6. Summary

The (^{3}He, t) charge-exchange reaction when studied with magnetic analysis at 0° represents a powerful tool for investigating IAS. Magnetic spectrometers provide excellent energy resolution, and the background from the beam stop inside the spectrometer can be kept very low when proper precautions are taken, even at bombarding energies of 200 MeV. The present data suggest that transitions to low-lying Gamow-Teller states and broad Gamow-Teller resonances in heavier nuclei can also be measured with high precision since the reaction mechanism at 0° is highly selective for $L = 0$ transitions.

Coincidence measurements between tritons detected in the focal plane of the magnetic spectrometer and decay protons detected in solid-state detectors near the target provide important information about the decay modes and branching ratios for IAS. They also yield much cleaner spectra for all proton-decaying states. Future coincidence measurements with decay neutrons may provide similar information for both IAS and high-lying giant resonances.

The present precision measurements of Q-values, line shapes and cross sections for transitions to IAS and branching ratios for proton decay have produced information about Coulomb displacement energies ΔE_{Coul}, decay widths Γ, escape and spreading widths, $\Gamma^{\uparrow}$ and $\Gamma^{\downarrow}$, and the effective interaction V_τ with emphasis on nuclei in the actinide region. The influence of deformed nuclear shapes on electrostatic energies is confirmed, estimates for the spreading widths due to isospin mixing of the IAS via coupling to the $T_<$-component of the IVGMR are confirmed, and an energy dependence of V_τ has been established.

The authors would like to acknowledge significant support by the technical staffs of the IUCF and KVI accelerator facilities, and in particular by C.C. Foster and W.R. Lozowski. The radioactive targets were made available by I. Ahmad (ANL) and J. van Klinken (KVI). This research was supported in part by the National Science Foundation Grants PHY-8605907 and PHY-8911831 (UM, Ann Arbor), PHY-8412177 (UM, Dearborn), and PHY-8714406 (IUCF). This work was also part of the research program of the "Stichting voor Fundamenteel Onderzoek der Materie" (FOM) with financial support from the "Nederlandse Organisatie voor Wetenschappelijk Onderzoek" (NWO). Essential travel support by the Scientific Affairs Division, North Atlantic Treaty Organization, travel grant NATO 85-0123, is gratefully acknowledged. One of the authors (JJ) thanks the organization FOM for financial support during several extended visits to the KVI. The hospitality extended by the KVI staff and in particular by R.H. Siemssen are highly appreciated.

References

1) C.D. Goodman, C.A. Golding, M.B. Greenfield, J. Rapaport, D.E. Bainum, C.C. Forster, W.G. Love and F. Petrovitch, Phys. Rev. Lett. **44** (1980) 1755

2) C.D. Goodman, *in* The (p, n) reaction and the nucleon-nucleon force, ed. C.D. Goodman, S.M. Austin, S.D. Bloom, J. Rapaport and J.R. Satchler (Plenum, New York, 1980) p. 149; Prog. Part. Nucl. Phys. **11** (1984) 475
3) F.D. Becchetti, W.S. Gray, J. Jänecke, E.R. Sugarbaker and R.S. Tickle, Nucl. Phys. **A271** (1976) 77
4) S.Y. van der Werf, N. Blasi, S. Brandenburg, A.G. Drentje, M.N.H Harakeh, W.A. Sterrenburg, B. Visscher and A. van der Woude, Phys. Lett. **B105** (1981) 111
5) J. Jänecke, E.H.L. Aarts, A.G. Drentje, M.N. Harakeh and C. Gaarde, Nucl. Phys. **A394** (1983) 39
6) J. Jänecke, F.D. Becchetti, W.S. Gray, R.S. Tickle and E. Sugarbaker, Nucl. Phys. **A402** (1983) 262
7) W.A. Sterrenburg, M.N. Harakeh, S.Y. van der Werf and A. van der Woude, Nucl. Phys. **A405** (1983) 109
8) W.A. Sterrenburg, S. Brandenburg, J.H. van Dijk, A.G. Drentje, M.B. Greenfield, M.N. Harakeh, H. Riezebos, H. Sakai, W. Segeth, S.Y. van der Werf and A. van der Woude, Nucl. Phys. **A420** (1984) 257
9) H.J. Hofmann, S. Brandenburg, P. Grasdijk, M.N. Harakeh, W.A. Sterrenburg and S.Y. van der Werf, Nucl. Phys. **A433** (1985) 181
10) G.W.R. Leibbrandt, Report KVI-115i (1986) p. 37
11) S.Y. van der Werf, S. Brandenburg, P. Grasdijk, W.A. Sterrenburg, M.N. Harakeh, M.B. Greenfield, B.A. Brown and M. Fujiwara, Nucl. Phys. **A496** (1989) 305;
P. Grasdijk, Ph.D. Thesis, University of Groningen (1986), unpublished
12) J.D. Anderson and C. Wong, Phys. Rev. Lett. **7** (1961) 250;
J.D. Anderson, C. Wong and J.W. McClure, Phys. Rev. **126** (1962) 2170
13) G.F. Bertsch and H. Esbensen, Rep. Prog. Phys. **50** (1987) 607
14) R. Schaeffer, Nucl. Phys. **A164** (1971) 145
15) F.D. Becchetti, W. Makofske and G.W. Greenlees, Nucl. Phys. **A190** (1972) 437
16) S.L. Tabor, G. Neuschaefer, J.A. Carr, F. Petrovitch, C.C. Chang, A. Guterman, M.T. Collins, D.L. Friesel, C. Glover, S.Y. van der Werf and S. Raman, Nucl. Phys. **A422** (1984) 12
17) I. Bergqvist, A. Brockstedt, L. Carlen, L.P. Ekström, B. Jakobson, C. Ellegaard, C. Gaarde, J.S. Larsen, C. Goodman, M. Bedjidian, D. Contardo, J.Y. Grossiord, A. Guichard, R. Haroutunian, J.R. Pizzi, D. Bachelier, J.L. Boyard, T. Hennino, J.C. Jourdain, M. Roy-Stephan, M. Boivin and P. Radvanyi, Nucl. Phys. **A469** (1987) 648
18) E. Comay and J. Jänecke, Nucl. Phys. **A410** (1983) 103;
J. Jänecke and E. Comay, Phys. Lett. **B140** (1984) 1
19) K. Ashktorab, S. Elitzur, J. Jänecke, S. Liran and N. Zeldes, Nucl. Phys. **A517** (1990) 27
20) J. Jänecke, M.N. Harakeh and S.Y. van der Werf, Nucl. Phys. **A463** (1987) 571
21) S.Y. van der Werf, M.N. Harakeh and E.N.M. Quint, Phys. Lett. **B216** (1989) 15
22) S.Y. van der Werf, M.N. Harakeh and J. Jänecke, 10th Biennale de Physique Nucleaire, Aussois, France, March 1989, p S 5.1
23) G.P.A. Berg, L.C. Bland, B.M. Cox, D. DuPlantis, D.W. Miller, K. Murphy, P. Schwandt, K.A. Solberg, E.J. Stephenson, B. Flanders and H. Seifer, IUCF Scientific and Technical Report, 1986
24) K. Solberg, A. Eads, J. Goodwin, P. Pancella, H.O. Meyer, T. Rinckel and A. Ross, Nucl. Instr. Meth. **A281** (1989) 283; IUCF Scientific and Technical Report, 1988
25) J.M. Schippers, W.T.A. Borghols and S.Y. van der Werf, Nucl. Instr. Meth. **A247** (1986) 467
26) A.G. Drentje, H.A. Enge and S.B. Kowalski, Nucl. Instr. Meth. **122** (1974) 485
27) F. Ajzenberg-Selove, Nucl. Phys. **A433** (1985) 43; Nucl. Phys. **A449** (1986) 1; Nucl. Phys. **A460** (1986) 1; Nucl. Phys. **A475** (1987) 1
28) P.M. Endt and C. van der Leun, Nucl. Phys. **A310** (1978) 1
29) B. Ramstein, L.H. Rosier and L. Jeanperrin, Nucl. Phys. **A317** (1979) 460
30) A.H. Wapstra, G. Audi and R. Hoekstra, At. Data Nucl. Data Tables **39** (1988) 281
31) C.F. von Weizsäcker, Z. Phys. **96** (1935) 431
32) H.A. Bethe and R.F. Bacher, Rev. Mod. Phys. **8** (1936) 82
33) H.A. Bethe, Phys. Rev. **54** (1938) 436
34) M.S. Antony, J. Britz and A. Pape, At. Data Nucl. Data Tables **40** (1988) 9
35) R.W. Hasse, Ann. of Phys. **68** (1971) 377
36) J. Jänecke, Phys. Lett. **B103** (1981) 1

37) S. Raman, C.H. Malarkey, W.T. Milner, C.W. Nestor and P.H. Stelson, At. Data Nucl. Data Tables **36** (1987) 1
38) A.Z. Mekjian, Nucl. Phys. **A146** (1970) 288
39) N. Auerbach, J. Hüfner, A.K. Kerman and C.M. Shakin, Rev. Mod. Phys. **44** (1972) 48
40) W.M. MacDonald and M.C. Birse, Phys. Rev. **C29** (1984) 425
41) N. Willis, I. Brissaud, Y. Le Bornec, B. Tatischeff and G. Duhamel, Nucl. Phys. **A204** (1973) 454
42) J.R. Comfort, Program DW81, updated 1983; extended version of DWBA70, R. Schaeffer and J. Raynal, unpublished
43) B.A. Brown and B.H. Wildenthal, private communication; B.H. Wildenthal, Prog. Part Nucl. Phys. **11** (1984) 5
44) W.A. Sterrenburg, S.M. Austin, V.E.P. Berg and R. DeVito, Phys. Lett. **B91** (1980) 337;
S.M. Austin, L.E. Young, R.R. Doering, R. DeVito, R.K. Bhomik and S.D. Schery, Phys. Rev. Lett. **44** (1980) 972;
T.N. Taddeucci, J. Rapaport, D.E. Bainum, C.D. Goodman, C.C. Foster, C. Gaarde, J. Larsen, G.A. Goulding, D.J. Horen, T. Masterson and E. Sugarbaker, Phys. Rev. **C25** (1981) 1094
45) W.G. Love and M.A. Franey, Phys. Rev. **C24** (1981) 1073
46) J.D. Bowman *et al.*, Phys. Rev. Lett. **50** (1983) 1195;
A. Erell *et al.*, Phys. Rev. Lett. **52** (1984) 2134;
A. Erell *et al.*, Phys. Rev. **C34** (1986) 1822;
E. Irom *et al.*, Phys. Rev. **C34** (1986) 2231
47) M.A. Moinester, A. Trudel, K. Raywood, S. Yen, R. Abegg, W.P. Alford, N. Auerbach, A. Celler, D. Frekers, O. Häusser, R.L. Helmer, R. Henderson, K.H. Hicks, K.P. Jackson, R.G. Jeppensen, N.S.P. King, S. Long, C.A. Miller, M. Vetterli, J. Watson and A.I. Yavin, Phys. Lett. **B230** (1989) 41
48) O. Bousshid, H. Machner, C. Alderliesten, U. Bechstedt, A. Djaloeis, P. Jahn and C. Meyer-Böricke, Phys. Rev. Lett. **12** (1980) 980
49) S. Gopal, A. Djaloeis, J. Bojowald, O. Bousshid, W. Oelert, N.G. Puttaswamy, P. Turek and C. Mayer-Böricke, Phys. Rev. **C23** (1981) 2459
50) E.H.L. Aarts, R.K. Bhowmik, R.J. de Meijer and S.Y. van der Werf, Phys. Lett. **B102** (1981) 307
51) D.C. Kocher, Nucl. Data Sheets **16** (1975) 55
52) J. Blachot and G. Marguier, Nucl. Data Sheet **50** (1987) 63
53) A. Hashizume, Y. Tendow and M. Oshima, Nucl. Data Sheet **52** (1987) 641
54) M.J. Martin, Nucl. Data Sheets **47** (1986) 797
55) W.J. Courtney and J.D. Fox, At. Data Nucl. Data Tables **15** (1975) 141
56) R. Meltzer, P. von Brentano and H. Paetz gen. Schieck, Nucl. Phys. **A432** (1985) 363